

# Infrared and radio study of star forming regions associated with IRAS 19111+1048 and IRAS 19110+1045

S. Vig<sup>1</sup>, S.K. Ghosh<sup>1</sup>, V.K. Kulkarni<sup>2</sup>, D.K. Ojha<sup>1</sup>, R.P. Verma<sup>1</sup>

1. *Tata Institute of Fundamental Research, Mumbai (Bombay) 400 005, India*

2. *National Centre for Radio Astrophysics, Pune 411 007, India*

sarita@tifr.res.in

## ABSTRACT

A multiwavelength study of the star forming regions associated with IRAS 19111+1048 and IRAS 19110+1045 has been carried out. These have been simultaneously mapped in two far infrared bands at  $\lambda_{eff} = 130$  and  $200 \mu\text{m}$  with  $\sim 1'$  angular resolution using the TIFR 1-m balloon borne telescope. The radio emission from the ionised gas of these regions has been imaged at 1280, 610 and 325 MHz using the Giant Metrewave Radio Telescope, India. A total of 20 compact radio sources have been detected from the high resolution radio map of IRAS 19111+1048 at 1280 MHz (of which one is of non-thermal origin). Assuming these sources to represent exciting zero age main sequence (ZAMS) stars, the initial mass function [ $\xi(m) \propto m^{-a}$ ] is found to be quite steep, with  $a = 5.3 \pm 0.5$  for the mass range  $14 < m/M_{\odot} < 33$ . The near infrared (NIR) source coincident with the IRAS peak is likely to be an embedded pre-main sequence star. An attempt has been made to identify sources responsible for ionising the gas using NIR sources from 2MASS. The spectral types of the ZAMS stars inferred independently from the radio and NIR measurements match very well for a good fraction of the radio sources having NIR counterparts. For the IRAS 19110+1045 region, seven radio sources have been detected of which two are associated with deeply embedded 2MASS objects. Self consistent radiative transfer modelling aimed at extracting important physical and geometrical details of the two IRAS sources has been carried out using the above cluster of ZAMS stars as the central exciting sources. The best fit models are in good agreement with the observed spectral energy distributions. A uniform density distribution of dust and gas is implied for both the sources. The extents of ionised gas, number of ZAMS stars, presence of deeply embedded sources and lower value of  $L/M$  for the cloud, support the youth of IRAS 19110+1045 vis-a-vis its neighbour, IRAS 19111+1048, consistent with earlier studies.

*Subject headings:* infrared: ISM – radio continuum: ISM – ISM: H II regions – ISM: individual (IRAS 19111+1048, IRAS 19110+1045)

## 1. Introduction

Massive stars are born deeply embedded in dense clouds of gas and dust. An outflow phase begins during early stage of stellar evolution. However, outflows have been more commonly seen among low mass stars than their massive counterparts (Shepherd 2005, and references therein). This is because the evolutionary time-scales of massive stars are much shorter. IRAS 19111+1048 (G45.12+0.13) and IRAS 19110+1045 (G45.07+0.13) are massive star forming regions from where bipolar molecular outflows have been detected (Hunter et al., 1997).

The H II region IRAS 19111+1048 is well-studied at many wavelengths as compared to the neighbouring H II region IRAS 19110+1045. Both these sources are at similar distances and a value of 6 kpc is assumed for the present work (Simon et al., 2001; Araya et al., 2002; Fish et al., 2003). According to Matthews et al. (1977), both the IRAS sources belong to the same star forming complex and are separated by  $\sim 3'.1$ . Kraemer et al. (2003) used the MIRAC3 instrument to obtain high angular resolution ( $\sim 1''$ ) images of the ultracompact sources associated with IRAS 19111+1048 and IRAS 19110+1045 in mid infrared (12.5 and 20.6  $\mu\text{m}$ ) as part of the Galactic Ring Survey (GRS) and resolved the IRAS 19110+1045 core into three compact sources and IRAS 19111+1048 core into two sources. Faison et al. (1998) have presented the infrared spectroscopy (3 – 13  $\mu\text{m}$ ) of these regions and have studied the silicate and polycyclic aromatic hydrocarbon (PAH) features as well as the [Ne II] line. They have also discussed dust shell models to explain the spectral energy distributions (SED).

Low resolution CO observations ( $\sim 6'$  by Israel, 1982;  $\sim 8'$  by Sanders et al., 1986) indicate that IRAS 19111+1048 is located at the extremities of a large, clumpy molecular cloud complex with IRAS 19111+1048 lying near the center of a well defined clump (Hoare et al, 1991). With higher angular resolution ( $\sim 20''$ ) CO observations (using the J= 3  $\rightarrow$  2 transition) Hunter et al. (1997) found that there are several spokelike protrusions from IRAS 19111+1048 core unlike the IRAS 19110+1045 core.

Wood & Churchwell (1989) observed a cometary shape for IRAS 19111+1048 and a compact unresolved source for IRAS 19110+1045 from their VLA survey at 5 and 15 GHz. High resolution ( $\sim 6''$  at 4.9 GHz &  $\sim 3''$  at 8.5 GHz) radio maps of these sources have been presented by Testi, Felli and Taylor, 1999 (hereafter TFT). From these maps, they

have extracted four compact sources from the IRAS 19111+1048 region and two from the IRAS 19110+1045. Extended radio emission has been seen around both these regions. Both regions contain Type I OH masers (Goss et al., 1973) but only IRAS 19110+1045 contains H<sub>2</sub>O maser (Genzel & Downes, 1977). Similarly, it was found that methyl cyanide was detected only towards IRAS 19110+1045 and not towards the other source (Pankonin et al., 2001). The presence of massive, bipolar molecular (CO) outflows from both these sources was discovered by Hunter et al. (1997). Based on lack of H<sub>2</sub>O and methyl cyanide masers near the IRAS 19111+1048 core as compared to IRAS 19110+1045 as well as multiple outflows and higher CO antenna temperatures, it is believed that of the two, IRAS 19111+1048 is a more advanced site of massive star formation.

In the present paper, we carry out a comparative study of these two regions using the infrared and radio observations. A multiwavelength study of these regions has been undertaken to gain further insight into the evolutionary states of these two regions. This is accomplished using the distribution of dust and ionised gas, dust optical depths, dust temperatures and spectral types of zero age main sequence (ZAMS) stars in these regions. While the dust around these regions is studied using the mid and far-infrared emission, the ionised gas in these regions is probed using the low frequency radio wavebands (1280, 610 and 325 MHz). The ZAMS spectral types are determined from the radio observations and near infrared (NIR) colour magnitude diagrams. Based on the spectral types determined from the radio observations, we estimate the slope of the initial mass function (IMF) for the IRAS 19111+1048 region.

In Section 2, we present the observations and other available data used for the present study. Section 3 describes the observational results. In Section 4, we present the radiative transfer models for the two IRAS sources. A comprehensive discussion of the multiwavelength study of these two regions is carried out in Section 5. Section 6 summarizes our results.

## 2. Observations and data reduction

### 2.1. Far infrared observations

The Galactic star forming region associated with IRAS 19111+1048 has been observed using two-band FIR photometer system at the Cassegrain focus of the TIFR 100 cm (f/8) balloon borne telescope. The observations were carried out during the balloon flight from the TIFR Balloon Facility, Hyderabad in India (latitude 17°.47 north, longitude 78°.57 east) on March 08, 1998. Details of the telescope and the observational procedure are given by Ghosh et al. (1988). A pair of 2×3 composite silicon bolometer arrays, cooled to 0.3 K

by liquid  $^3\text{He}$ , corresponding to the two FIR bands are used to view identical parts of the sky simultaneously. The field of view of each detector is  $1'.6$ . The in-flight parameters of the telescope optics, necessary to establish point spread functions etc, were determined from an optical detector array (Photodiode array) in the Cassegrain focal plane of the telescope. Details of the optical instrument can be found elsewhere (Naik et al., 2000). The spectral response of each of the bands of the FIR photometer was determined in the laboratory using a Michelson interferometer and a Golay cell as a comparison detector. Hereafter, the two TIFR bands will be referred to as 130 and 200  $\mu\text{m}$  bands corresponding to the  $\lambda_{eff}$  for a modified blackbody source of temperature 25 K and  $\lambda^{-2}$  emissivity law.

The regions around IRAS 19111+1048 and IRAS 19110+1045 were mapped by raster scanning the region of the sky ( $\sim 30' \times 26'$ ) in cross-elevation with steps in elevation at the end of each scan. The sky chopped FIR signals were gridded into a matrix with pixel size  $0'.3 \times 0'.3$ . The deconvolution of the observed signal matrix is carried out using the maximum entropy method similar to that of Gull & Daniell (1978) (for details see Ghosh et al., 1988). Absolute positional accuracy of  $\sim 0'.8$  (Naik et al., 2000) and angular resolution of  $\sim 1'$  have been achieved in the FIR maps using this method.

## 2.2. Radio observations

The radio continuum observations in three frequency bands, 1280, 610 and 325 MHz were carried out using the Giant Metrewave Radio Telescope (GMRT), India. The GMRT has a “Y” shaped hybrid configuration of 30 antennas, each of 45 m diameter. Six antennas are placed along the three arms (east, west and south) and twelve antennas are located in a random but compact  $1 \times 1 \text{ km}^2$  pattern at the centre (Swarup et al., 1991). The baselines ( $\sim 100 \text{ m} - 25 \text{ km}$ ) provide sensitivity to large scale diffuse emission as well as high angular resolution. The observational details are listed in Table 1.

For the observations, the primary flux density calibrators used were 3C48 and 3C286. Since IRAS 19111+1048 and IRAS 19110+1045 are separated by a distance of  $3'.1$ , both lie within the primary beam of the telescope at all the frequencies. Hence, interferometric mapping with one phase center has been carried out for both the sources. NRAO Astronomical Image Processing System (AIPS) was used for data reduction. The data were carefully checked for RF interference or other problems and suitably edited. The calibrated data are Fourier transformed and deconvolved using the IMAGR task in AIPS. Self calibration was carried out to remove the residual effects of atmospheric and ionospheric phase corruptions and obtain the improved maps. For the lower frequency (325 and 610 MHz) images, the system temperature was obtained using the sky temperature from 408 MHz map of Haslam

et al. (1982). A correction factor equal to ratio of the system temperature towards the source has been used to scale the deconvolved images. For the sources detected ( $S/N > 10$ ) in the radio maps, the peak position as well as the flux densities (peak and integrated) were obtained using the task JMFITS in AIPS.

### 2.3. Other available datasets

Other available data (2MASS, IRAS, MSX, ISO, JCMT) for the regions around IRAS 19111+1048 and IRAS 19110+1045 have been used to study them at different wavelengths ( $1.2 - 850 \mu\text{m}$ ). The flux densities from the images have been used for the construction of the SED in order to extract physical parameters of the star forming regions using radiative transfer modelling (see Section 4). The 2MASS point sources and images have been used to identify the sources of ionisation of gas in these regions.

#### 2.3.1. IRAS

The data from the Infrared Astronomical Satellite (IRAS) survey in the four bands (12, 25, 60 and  $100 \mu\text{m}$ ) for IRAS 19111+1048 and IRAS 19110+1045 were HIRES (High Resolution processing using Maximum Correlation Method; Aumann et al., 1990) processed at the Infrared Processing and Analysis Center (IPAC, Caltech) to obtain high angular resolution maps ( $0'.5 \times 1'.0$  at  $12 \mu\text{m}$ ,  $0'.5 \times 1'.1$  at  $25 \mu\text{m}$ ,  $1'.0 \times 1'.6$  at  $60 \mu\text{m}$ ,  $1'.9 \times 2'.3$  at  $100 \mu\text{m}$ ). Apart from extracting the sources and determining the flux densities, the IRAS-HIRES maps at 12 and  $25 \mu\text{m}$  have been used to find the spatial distribution of temperature,  $T(12/25)$ , and optical depth at  $25 \mu\text{m}$  ( $\tau_{25}$ ).

IRAS 19111+1048 appears in IRAS Low Resolution Spectrometer (LRS) Catalog (IRAS Science Team, 1986) and the spectrum of this source in the wavelength range  $8 - 22 \mu\text{m}$  has been used for constructing the SED.

#### 2.3.2. MSX

The Midcourse Space Experiment<sup>1</sup> (MSX) surveyed the entire Galactic plane within  $|b| \leq 5^\circ$  in four mid infrared wavebands: 8.3, 12.1, 14.7 and  $21.3 \mu\text{m}$  at a spatial resolu-

---

<sup>1</sup>This research made use of data products from the Midcourse Space Experiment. Processing of the data was funded by the Ballistic Missile Defense Organization with additional support from NASA Office of Space

tion of  $\sim 18''.3$  (Price et al., 2001). The panoramic images of the Galactic plane survey of MSX were taken from IPAC (<http://irsa.ipac.caltech.edu/applications/MSX/>). These MSX maps were used to extract the sources and determine their flux densities for constructing the SED. Point sources close to these star forming regions have been selected from MSX Point Source Catalog Version 2.3 (Egan et al., 2003) and cross-correlated with 2MASS sources.

### 2.3.3. 2MASS

The point sources around the regions IRAS 19111+1048 and IRAS 19110+1045 were extracted from the Two Micron All Sky Survey<sup>2</sup> (2MASS) Point Source Catalog (PSC). The 2MASS PSC is complete down to  $J \leq 15.8$ ,  $H \leq 15.1$  and  $K_s \leq 14.3$  mag for  $S/N > 10$ , in the absence of confusion. The J, H and  $K_s$  magnitudes of the extracted sources have been used to make colour-magnitude diagrams which, in conjunction with the radio observations, are used to identify the sources responsible for ionisation of gas in these regions. The JHK<sub>s</sub> magnitudes and images were taken from IPAC (<http://www.ipac.caltech.edu/2mass/>).

### 2.3.4. ISO

For IRAS 19110+1045, the data from the Short Wavelength Spectrometer (de Graauw et al., 1996) and the Long Wavelength Spectrometer (Clegg et al., 1996) of the Infrared Space Observatory<sup>3</sup> (ISO) between 2 – 188  $\mu\text{m}$  have been used for constructing the SED of this source. The version of the ISO data used in this paper correspond to the Highly Processed Data Product (HPDP) sets called ‘A uniform database of SWS 2.4-45.4 micron spectra’, ‘High resolution processed and defringed SWS01s’ and ‘Uniformly processed LWS L01 spectra’ by Sloan et al. (2003), Frieswijk et al. (2004) and Lloyd et al. (2003) respectively, obtained from the ISO Data Archive.

---

Science. This research has also made use of the NASA/ IPAC Infrared Science Archive, which is operated by the Jet Propulsion Laboratory, Caltech, under contract with the NASA.

<sup>2</sup>This publication makes use of data products from the Two Micron All Sky Survey, which is a joint project of the University of Massachusetts and the Infrared Processing and Analysis Center/California Institute of Technology, funded by the NASA and the NSF.

<sup>3</sup>Based on observations with ISO, an ESA project with instruments funded by ESA Member States (especially the PI countries: France, Germany, the Netherlands and the United Kingdom) and with the participation of ISAS and NASA.

### 2.3.5. JCMT

Submillimeter observations using the Submillimetre Common-User Bolometer Array (SCUBA) instrument of James Clark Maxwell Telescope<sup>4</sup> (JCMT) of IRAS 19111+1048 and IRAS 19110+1045 were obtained from the JCMT archive and processed using their standard pipeline SCUBA User Reduction Facility (SURF). Maps generated at 450 and 850  $\mu\text{m}$  were used to extract the sources and determine their flux densities for constructing the SEDs.

## 3. Results

### 3.1. Emission from cold dust

The deconvolved TIFR far-infrared maps at 130 and 200  $\mu\text{m}$  bands are presented in Fig 1. The sources corresponding to IRAS 19111+1048 and IRAS 19110+1045 are resolved in the 130  $\mu\text{m}$  map and an extension corresponding to IRAS 19110+1045 can be seen in the 200  $\mu\text{m}$  map. The flux densities of both the sources at 130  $\mu\text{m}$ , and of IRAS 19111+1048 at 200  $\mu\text{m}$  obtained by integrating over circular regions of diameter  $3'$ , centered on the far infrared peaks, are listed in Table 2. These far infrared wavebands probe the distribution of cold dust around this region. The colour temperature of dust is obtained as  $\sim 34$  K for this region ( $\sim 3'$ ) using a dust emissivity law,  $\epsilon_\lambda \propto \lambda^{-2}$  and assuming that the dust is optically thin.

The JCMT maps of these sources at 450 and 850  $\mu\text{m}$  detect the cold dust around these regions. The distribution of the emission from dust at these wavelengths is shown in Fig 2. The maps at 450 and 850  $\mu\text{m}$  correspond to beam sizes of  $\sim 7'' \times 11''$  and  $\sim 13'' \times 17''$ , respectively.

### 3.2. Emission from warm dust

The HIRES processed maps of IRAS 19111+1048 and IRAS 19110+1045 at 12, 25, 60 and 100  $\mu\text{m}$  are shown in Fig 3, where both the sources are clearly resolved. Table 2 lists the flux densities determined from the HIRES maps. The IRAS PSC flux densities of these sources in all four wavebands are also presented for comparison.

---

<sup>4</sup>This paper makes use of data from the James Clarke Maxwell Telescope (JCMT) Archive. The JCMT is operated by the Joint Astronomy Centre on behalf of the UK Particle Physics and Astronomy Research Council, the National Research Council of Canada and the Netherlands Organisation for Pure Research.

We have used the IRAS-HIRES maps at 12 and 25  $\mu\text{m}$  to generate the spatial distributions of dust colour temperature,  $T(12/25)$  and optical depth at 25  $\mu\text{m}$  ( $\tau_{25}$ ). The emissivity law of  $\epsilon_\lambda \propto \lambda^{-1}$  was assumed to generate these maps. It may be noted that the spatial distribution of temperature is insensitive to the assumed value of the emissivity exponent. These wavelengths probe the warm (100 – 160 K) dust in the region around IRAS 19111+1048 and IRAS 19110+1045. The peak optical depth at 25  $\mu\text{m}$  is 0.001 located at the peak infrared emission of IRAS 19111+1048. We have presented the distribution of  $\tau_{25}$  as contours in Fig 4.

The emission in mid infrared from warm dust, in the MSX 8.3  $\mu\text{m}$  band, towards these sources is shown in Fig 5 (left). The flux densities from the four MSX maps integrated for circular regions with 3' diameter around IRAS 19111+1048 and IRAS 19110+1045 are listed in Table 2. We have modelled the thermal continuum from the interstellar dust alongwith the emission in the Unidentified Infrared Bands (UIBs), using the data from MSX in the 8, 12, 14 and 21  $\mu\text{m}$  bands, following the scheme developed by Ghosh & Ojha (2002). The peak strength of the modelled UIB emission is  $5.8 \times 10^{-4} \text{ W m}^{-2} \text{ Sr}^{-1}$  at the position of IRAS 19111+1048. The spatial distribution of UIB emission resembles that of the continuum emission from warm dust at 8.3  $\mu\text{m}$ . Faison et al. (1998) carried out infrared spectroscopy of central regions ( $\sim 9''$ ) of both these sources but have not detected the PAH features. The peak PAH emission obtained from MSX is  $\sim 5$  times the noise level of Faison et al. (1998). As the resolution of MSX is  $\sim 18''$ , it is likely that the UIB/PAH emission has a shell type distribution as seen in other star forming regions (Darbon et al. 2000). The temperature of the mid infrared emitting dust is found to be in the range 100-160 K (consistent with that obtained from IRAS-HIRES T(12/25)), the spatial distribution of which is presented as isotherms in Fig 5 (right).

### 3.3. Emission from ionised gas

The radio continuum emission from the region around IRAS 19111+1048 and IRAS 19110+1045 at 1280 MHz is shown in Figs 6 and 7, respectively. The corresponding maps at 610 and 325 MHz are shown in Figs 8 and 9, respectively. The synthesized beam sizes and the rms noise in the maps are given in Table 1. As can be seen from the radio emission maps at 1280 MHz, 20 discrete sources have been detected in the region around IRAS 19111+1048 and 7 in the IRAS 19110+1045 region (with S/N > 10). A list of these sources along with their peak and integrated flux densities at 1280 and 610 MHz are presented in Tables 3 and 4. We designate these sources as S1, S2, ... , S27. The total integrated flux densities for IRAS 19111+1048 at 1280, 610 and 325 MHz are  $6.60 \pm 0.01$ ,  $3.90 \pm 0.01$  and  $0.8 \pm 0.02$



Jy, respectively. The extent of ionised gas of the H II region IRAS 19111+1048 is  $\sim 2.8$  pc while that of IRAS 19110+1045 is  $\sim 1.3$  pc. The flux density measurement of IRAS 19111+1048 was carried out by Altenhoff et al. (1979) at 4.875 GHz with the Effelsberg 100-m telescope (beam  $\sim 2'.6$ ). Scaling this measurement to 1.280 GHz under the assumption that it is optically thin at both these frequencies, we find that with the interferometer, we have collected  $\sim 95\%$  of the total flux density as measured with the single dish demonstrating that almost all structural features have been captured by the baselines of GMRT. For IRAS 19110+1045, the total integrated flux densities are  $730 \pm 6$  mJy,  $552 \pm 6$  mJy &  $110 \pm 4.3$  mJy at 1280, 610 & 325 MHz, respectively.

Assuming that each discrete source in the radio continuum maps represents an exciting ZAMS star, the spectral types of the sources have been estimated using the integrated flux densities from our GMRT maps and the formulation of Schraml & Mezger (1969) and Panagia (1973). The ZAMS spectral types determined in this way are listed in Tables 5 and 6. As can be seen all the sources are earlier than B0.5. For the sources also detected by TFT, we have compared the spectral types obtained from our GMRT maps as well as from the flux densities given by TFT and these are found to be consistent (see Tables 5 and 6).

### 3.3.1. Physical properties of the compact cores

The physical properties like the electron temperature and emission measure of the compact core of IRAS 19111+1048 (shown as ‘14’ in Fig 6 and S14 in Table 3) can be estimated using the flux densities of the unresolved core at low frequencies (1280 and 610 MHz from the GMRT images) as well as at higher frequencies (4.9 and 8.5 GHz using the listed parameters of this core from Table 1 of TFT). Under the approximation that the core is homogeneous and spherically symmetric, the flux density,  $S$ , (Mezger & Henderson, 1967) is given by

$$S = 3.07 \times 10^{-2} T_e \nu^2 \Omega (1 - e^{-\tau(\nu)})$$

$$\tau(\nu) = 1.643 \times 10^5 a \nu^{-2.1} (EM) T_e^{-1.35}$$

where  $S$  is the integrated flux density in Jy,  $T_e$  is electron temperature in K,  $\nu$  is the frequency in MHz,  $\tau$  is the optical depth,  $\Omega$  is the solid angle subtended by the source in Steradian (which in this case is the synthesized beam size for the unresolved core), and  $EM$  is the emission measure in  $\text{cm}^{-6}\text{pc}$ . The factor  $a$  represents the deviation between the exact formulation and its approximation. We use  $a = 0.99$  obtained from Table 6 of Mezger & Henderson (1967) for the frequency range 0.6 – 8 GHz for  $T = 10,000$  K. The peak flux densities of the cores after convolving the images to a common resolution ( $10'' \times 10''$ ) have been used to fit the above equations using nonlinear least-squares Marquardt-Levenberg

algorithm. The observed and the best fit model flux densities are shown in Fig 10. For the best fit model, the electron temperature and emission measure (with  $1\sigma$  errors) of the IRAS 19111+1048 core are  $8346 \pm 1511$  K and  $8.8 \pm 0.7 \times 10^6$  cm<sup>-6</sup>pc, respectively. Wood & Churchwell (1989) used the H76 $\alpha$  recombination line to obtain the electron temperature of  $7900 \pm 1000$  K which is consistent with our value within errors. Using radio continuum emission at 15 GHz, they obtained the peak ( $0''.4 \times 0''.4$ ) values of electron temperature and emission measure to be 8100 K and  $1.5 \times 10^9$  cm<sup>-6</sup>pc, respectively. The difference in *EM* values could be due to clumpy distribution of ionised gas. Lumsden & Puxley (1996) obtained an electron temperature of 8000 – 9000 K by means of a best fit to the near infrared spectrum of IRAS 19111+1048 core.

The compact cores S26 and S27 belonging to IRAS 19110+1045 region are resolved at 1280 MHz but not at 610 MHz. They are, however, resolved in the 4.9 and 8.5 GHz maps of TFT. While S26 appears to be optically thin at these three frequencies (1280 MHz, 4.9 GHz and 8.5 GHz), S27 appears to be optically thick. For an assumed temperature of 8000 K, the best fit emission measure for S26 is  $2.5 \pm 0.3 \times 10^5$  cm<sup>-6</sup>pc. Since S27 is a compact unresolved source at all these three frequencies, we estimate the size of S27 to be 0.026 pc using the flux density at 1280 MHz for a similar temperature. Assuming photon bounded uniform density region, this size implies electron density,  $n_e = 1.5 \times 10^4$  cm<sup>-3</sup>. Garay et al. (1986) modelled this source as an ionised toroid of size 0.03 pc (scaled to our distance) and obtained  $n_e = 1.6 \times 10^5$  cm<sup>-3</sup>, which are comparable.

### 3.4. Embedded star cluster

With the aim of identifying early type stars in the embedded cluster of the two H II regions, we study the NIR point sources from 2MASS PSC in the J, H and K<sub>s</sub> bands. In this section, we discuss the nature of these sources. We have used the colour-magnitude (CM) diagrams of sources in the regions around IRAS 19111+1048 and IRAS 19110+1045 to estimate the spectral types of the stars. For IRAS 19111+1048, 47 stars were found in a circle of radius 1'.2 around the center of the radio emission ( $\alpha_{2000} = 19^h 13^m 26.0^s$ ,  $\delta_{2000} = +10^\circ 54' 11''$ ) which were detected in all the three JHK<sub>s</sub> bands of 2MASS. All the sources whose magnitudes are given as upper limits have been excluded from the study. A similar study was carried out for the source IRAS 19110+1045. Within a circle of radius 1' around this source ( $\alpha_{2000} = 19^h 13^m 20.6^s$ ,  $\delta_{2000} = +10^\circ 50' 47''$ ), 42 stars were detected in all the three 2MASS bands. A list of the positions and apparent magnitudes of the 2MASS sources that are likely to be associated with the radio sources of IRAS 19111+1048 and IRAS 19110+1045 regions (see Section 5) is presented in Table 7. The CM diagrams (J-H

vs J) for the sources detected in 2MASS JHK<sub>s</sub> bands around IRAS 19111+1048 and IRAS 19110+1045 regions are shown in Fig 11. The nearly vertical solid lines from left to right represent the ZAMS curves (for a distance of 6 kpc) reddened by  $A_V = 0, 15$  and  $30$  mag, respectively. The slanting lines trace the reddening vectors of these zero main sequence stars. We have assumed extinction values of  $A_J/A_V = 0.282$ ,  $A_H/A_V = 0.175$  and  $A_{K_s}/A_V = 0.112$  from Rieke & Lebofsky (1985). All the 2MASS magnitudes as well as the ZAMS curves are in the Bessel & Brett (1988) system. In Fig 11, the triangles (IR4, IR8) represent sources which are very bright in K<sub>s</sub> band and lie much higher than the extinction curve of O5 star, possibly embedded or unresolved stellar objects. The asterisk symbols represent sources of spectral type B0 or earlier and lying within the radio nebulosity. The plus symbols represent stars of spectral type later than B0 but found within the radio nebulosity. The dot symbols represent sources which do not lie within the radio nebulosity.

#### 4. Radiative transfer modelling

With the aim of extracting important physical parameters, an attempt has been made to construct radiative transfer models of the two sources IRAS 19111+1048 and IRAS 19110+1045. Although high resolution maps in radio and NIR indicate the presence and location of a cluster of sources, we carry out simplistic radiative transfer modelling assuming a cluster of ZAMS stars located at the center of a spherically symmetric homogeneous cloud of gas and dust. This cloud is assumed to be immersed in an isotropic radiation field (typical Interstellar Radiation Field, ISRF). The self-consistent scheme developed by Mookerjea and Ghosh, (1999) has been used here.

The physical parameters explored to get a fit to the SED are: the nature of the embedded source (single or a cluster of ZAMS stars of appropriate initial mass function and mass limits), radial density distribution law [ $n(r) \propto r^{-\alpha}$ ,  $\alpha = 0, 1, 2$ ], relative abundances of the two constituent grain types (silicate and graphite), the total radial optical depth due to the dust, the gas-to-dust ratio by mass and geometric details of the cloud (e.g. cavity size, outer size of the cloud). Two commonly used types of interstellar dust are explored: the type of dust grains from Draine & Lee, (1984; DL) and the dust type from Mathis, Mezger & Panagia, (1983). The observed angular sizes have been used to constrain the models.

#### 4.1. IRAS 19111+1048

The SED for IRAS 19111+1048 has been constructed using the flux densities obtained from the MSX maps, the IRAS-LRS data, the IRAS-HIRES maps, the TIFR maps, the submillimeter (450 and 850  $\mu\text{m}$ ) JCMT-SCUBA maps. The SED also includes the flux densities in the J, H and  $K_s$  bands obtained by integrating the fluxes of the 2MASS sources within a circle of diameter  $3'$  centered on the peak of IRAS 19111+1048. The total luminosity obtained by integrating the observed SED is  $6.5 \times 10^5 L_\odot$ . We have used a cluster of 19 ZAMS OB stars, obtained from our radio measurements (first 19 sources listed in Tables 3 and 5, S20 being a non-thermal source; see Section 5 for more details), as the centrally exciting sources which power this region. The total luminosity of this cluster is  $8.5 \times 10^5 L_\odot$ . Modelling the SED of IRAS 19111+1048 gives a better fit for uniform ( $r^0$ ) density distribution than for the other two power laws. The outer radius of the spherical cloud is 4 pc and radius of the dust cavity  $\sim 0.01$  pc. The preferred dust is of DL type with radial optical depth of 0.002 at 100  $\mu\text{m}$ . We have used the radius of the H II region (1.4 pc) from our 1280 MHz map to constrain the gas-to-dust ratio by mass, which is obtained to be 250. This implies an under-abundance of dust grains in this region. The radio continuum emission predicted by this model at 1280 MHz is 3.8 Jy which is  $\sim 60\%$  of the observed value. The best fit model along with the SED is shown in Fig 12. The predicted emission from the model at wavelengths shorter than  $\sim 2 \mu\text{m}$  is dominated by the scattered ISRF due to dust grains in the cloud. IRAS 19111+1048 is unresolved at the MSX and IRAS-HIRES wavebands; this is consistent with the sizes obtained from the model. The expected angular sizes of IRAS 19111+1048 in the TIFR maps have been estimated from the model by convolving the predicted source size at that band with the achieved angular resolution. This is consistent with the sizes seen at 130 and 210  $\mu\text{m}$ . The various parameters of the best-fit model are listed in Table 8.

#### 4.2. IRAS 19110+1045

For IRAS 19110+1045, the ISO-SWS and ISO-LWS spectra from 3 to 188  $\mu\text{m}$  are available. The radiative transfer modelling uses the flux densities obtained from the JCMT-SCUBA maps at 450 and 850  $\mu\text{m}$  bands to carry out radiative transfer modelling for this source. The SED also includes the total emission from 2MASS sources within the equivalent beam of ISO-SWS, in the J, H, and  $K_S$  bands. From our radio maps, seven radio sources have been extracted from this region (see Table 6). In our model, we have used these as the central exciting sources. ISO-SWS spectrum covers the wavelength range 2 – 45  $\mu\text{m}$  corresponding to a field of view (FOV)  $33'' \times 20''$ . On the other hand, the ISO-LWS spectrum

covers wavelengths longer than  $\sim 45 \mu\text{m}$  with a FOV of diameter  $84''$ . For comparing the radiative transfer model results with the LWS and SWS data, the model results have been convolved with the appropriate beams. Consequently, we see a slight discontinuity in the SED at  $\sim 45 \mu\text{m}$ . We obtain the total luminosity to be  $3.3 \times 10^5 L_\odot$  by integrating the observed SED. However the total luminosity of the resolved stars is  $1.1 \times 10^5 L_\odot$ . Guided by the composition of the observed radio spectral types as well as the luminosity obtained by integrating the SED, we carry out radiative transfer modelling. The data and the best fit model are shown in Fig 13. The model fits the observations reasonably well. The model fitted to the observed SED best corresponds to a constant density cloud. The radio continuum flux density predicted by the model underestimates the observed flux density by a factor of 3 at 1280 MHz but matches the flux density at 8.3 GHz (TFT) of 0.84 Jy for a gas-to-dust ratio of 450. This gas-to-dust ratio is rather large. The radius of the H II region predicted by this model is 0.04 pc while the radius of the region encompassing S21-S25 is found to be  $\sim 0.9 - 1.1$  pc at 1280 MHz and 4.9 GHz. The large gas-to-dust ratio and the difference in the size of the HII region from the model and observations implies significant difference of the true geometry of the source from the simple assumptions used in the modelling. It is likely that the medium is clumpy. The DL type of dust fits the data better. Table 8 lists the various parameters of the best-fit model to the SED.

## 5. Discussion

### 5.1. IRAS 19111+1048

The far infrared IRAS-HIRES, TIFR and JCMT-SCUBA maps probe the cold dust environment around IRAS 19111+1048. The flux densities from the JCMT-SCUBA maps at 450 and 850  $\mu\text{m}$  have been used to compute the mass of dust using the formulation of Hildebrand (1983) and Sandell (2000). The dust mass obtained from emission at 450 and 850  $\mu\text{m}$  is  $\sim 20 M_\odot$  while that obtained from 200  $\mu\text{m}$  emission map is  $18 M_\odot$ . A dust mass of  $12 M_\odot$  is obtained from the radiative transfer modelling. This compares well with the dust mass of  $24 M_\odot$  obtained by Hoare et al., 1991, (scaled to our distance) from the submillimeter observations. Considering a gas-to-dust ratio of 250 by mass from the radiative transfer model (see Section 4.1), we determine the gas mass in this region to be  $5,000 M_\odot$ .

The optical depth at 100  $\mu\text{m}$  obtained from radiative transfer modelling is,  $\tau_{100} \sim 0.002$ . This could be compared with the peak value of optical depth at 25  $\mu\text{m}$  obtained from the IRAS-HIRES maps,  $\tau_{25} \sim 0.001$ . The apparent inconsistency of the lower value of  $\tau_{25}$  as compared to  $\tau_{100}$  can be resolved by attributing the  $\tau_{25}$  to warmer dust of smaller volume around the exciting sources. Faison et al. (1998) modelled the dust distribution around this

source and obtained a value of  $\tau_{100} = 0.01$ . This discrepancy can be attributed to (i) distance of 9.7 kpc used by them, and (ii) their model fits only the mid-infrared spectrum reasonably well and not the full SED.

The radio emission of this H II region indicates the extent of ionised gas. As can be seen from all the radio maps, a number of sources have been detected apart from diffuse emission. A comparison with the high resolution maps of TFT at 4.9 and 8.5 GHz indicates that our source list includes all the four sources detected by them. The compact sources detected by them around this UC H II region are listed as sources 13, 15, 16 and 17 in their Table 1. We shall designate these sources as TFT13, TFT15, TFT16 and TFT17, respectively. A positional comparison of their sources and those detected by us at 1280 MHz indicates that TFT13 can be identified with S6, TFT15 with S14, TFT16 with S18 and TFT17 with S19 (Table 5). The diffuse emission corresponding to TFT31 is emission to the north-west of S14 in our maps which has been resolved into multiple sources here. A comparison between the 1280 and 610 MHz maps show that many sources which have been detected in the former are not resolved in the latter.

For the point source S20, we find that the flux density at 610 MHz is higher than the flux density at 1280 MHz band corresponding to a power law spectral index of -0.6. This indicates non-thermal nature of the radio emission. Assuming this spectral index, the expected flux densities at 4.9 and 8.5 GHz are 8.6 mJy and 6.2 mJy, respectively. The absence of this source from the maps of TFT is consistent with the lowest peak values of the compact sources listed in their Table 1: 17 mJy/beam at 4.9 GHz and 24 mJy/beam at 8.5 GHz. Though S20 is in the vicinity of IRAS 19111+1048, it is unlikely to be associated with IRAS 19111+1048 and consequently, we shall not consider S20 as a part of this H II region for further analysis. In the 325 MHz image, we do not see this source due to resolution effect though an extension corresponding to this source can be seen.

Using the 19 radio sources, we find the slope of the initial mass function [ $\xi(m) \propto m^{-a}$ ] in this star forming region to be  $a = 5.3 \pm 0.5$  in the mass range  $14 < m/M_{\odot} < 33$ . The initial mass function is quite steep implying a scarcity of massive and luminous stars in this region. Such a steep power law of the initial mass function is characteristic of young star forming regions. For example, Ghosh et al. (1989) obtained  $a = 6$  and 3 for the regions W31 and W33, respectively, for  $20 < m/M_{\odot} < 35$  using a similar analysis.

We now identify the NIR counterparts of these radio sources using the position information ( $< 2''.5$ ; resolution of 1280 MHz map) from the 2MASS NIR images and catalogs. We designate these NIR sources as IR1, IR2, ... , IR7 (Table 7). The 1280 MHz radio contours are plotted over the 2MASS  $K_s$ -band image, shown in Fig 14. Some of the radio sources with their possible ionisation sources from NIR (position and colour) are also compared in Table

5. Six sources have been identified of which the spectral types deduced from radio emission of the three sources, S6, S11 and S14, agree quite well with the spectral types obtained from NIR measurements. We have also checked for positional match of the radio sources with sources detected in H &  $K_s$  bands or only in  $K_s$  band. We find only one such match for S4 which is detected in only  $K_s$  band (mag  $\sim 14.1$ ).

The compact H II source, S14, is deduced to be of spectral type O6 from the integrated radio emission. There are two NIR objects, IR4 and IR5, within S14 region as obtained from the NIR catalog and images. IR4 is at the peak of the radio emission and matches the OH maser position ( $\alpha_{2000} = 19^h 13^m 27.8^s$ ,  $\delta_{2000} = +10^\circ 53' 37''$ ) obtained by Argon et al. (2000). IR4 is very bright in  $K_s$ -band (mag  $\sim 7.9$ ) and appears to be of spectral type much earlier than O5 as indicated by a triangle in the CM diagram. It could be an embedded pre-main sequence star or it is likely to comprise of two or more unresolved early type stars. Hunter et al. (1997) detected two sources of CO bipolar outflow; one of which is at the location of the radio peak IR4. Considering the facts: (a) IR4 is coincident with the OH maser position, (b) it is the source of bipolar outflow, and (c) has large infrared excess (J-K  $\sim 4.0$ ), it is likely that this source could be an embedded pre-main sequence object. The ionisation of gas could also be attributed to IR5, which according to our CM diagram is of stellar type O5. It is interesting to note that although the source S14 peaks at the position of IRAS source, the radio morphology in all the three GMRT bands, shows a north-south extension indicating that perhaps this is not a single compact core but rather has more than one H II clump. This is also clearly evident from the maps of TFT. Kraemer et al. (2003) find that the IRAS 19111+1048 core consists of two compact mid infrared (12.5 and 20.6  $\mu\text{m}$ ) components. If we consider sources only detected in the  $K_s$  band within the S14 region, we find that there are four more NIR sources detected. It thus appears that the source S14 has a compact embedded cluster and is perhaps a conglomeration of H II clumps, the brightest one at the position of S14.

For the sources S6, S11 and S14, the spectral types obtained from radio measurements and NIR colours agree very well. However, the agreement is not good for S16, S19 and S12. S16 and S19 are found to be of spectral types B0.5-B0 and B0-O9.5, respectively. They are associated with IR6 & IR7, respectively, which are of spectral type B7-B3 obtained from the NIR CM diagram. Most probably, IR6 and IR7 are reddened main sequence foreground sources based on their position in the CM diagram. For S12 also, we find that the radio and NIR spectral types do not match. While the radio spectral type of the ZAMS star is O8, the NIR counterpart is of spectral type B2. These three cases could be spurious associations. This number of spurious associations can be compared with the estimated number of chance associations of 1.3 obtained by considering the density of NIR sources (detected in H and  $K_s$  bands) and the search radius  $\sim 2''.5$  of the 19 radio sources.

From the NIR CM diagram, we see that most of the ZAMS stars within the radio nebulosity have extinction values corresponding to  $A_V \sim 10\text{--}35$  mag. This is quite consistent with the extinction values obtained ( $A_V = 10 - 30$ ) by Hoare et al. (1991). Lumsden & Puxley, (1996) obtained  $A_V \sim 24$  from Br- $\gamma$  imaging and radio continuum observations for this source.

Although the radio and NIR  $K_s$ -band images indicate positional match for some radio and NIR sources (with consistent spectral types), there are a number of radio sources which do not have a NIR counterpart. The radio spectral types indicate that these are bright sources which ought to have been detected in NIR. Their absence gives rise to two possibilities: (1) the radio sources are high density ionised clumps with no centrally exciting star or (2) the medium is clumpy with dense distributions of  $A_V > 30$ , while the average visual extinction is lower ( $A_V \sim 15$ ). Next, we show that the first scenario of high density clumps being ionised by ZAMS stars located away from them can be ruled out. For instance, S13 does not have a NIR counterpart. An estimation of the Lyman continuum photons reaching S13 from its neighbour S14 (the brightest source in this region; see Fig 6) due to geometrical factors shows that, in the absence of any intervening medium, the expected luminosity is only 5% of its observed luminosity. Hence, it is more likely that the second scenario is responsible for the non-detection of the NIR counterparts. A high resolution mapping of molecular species probing the cold and dense gas over a large region ( $\sim 1.5'$ ) around this source is required to better our understanding of the physical picture of this region. The radio morphology towards the north-east of the extended radio emission indicates steepness of the gradient of the radio emission. This could be due to the restriction of the ionised region by molecular gas, as seen in other regions like S201 (Ojha et al., 2004a) and NGC7538 (Ojha et al., 2004b).

We have also cross-correlated the MSX PSC sources with those from 2MASS PSC which lie within the radio nebulosity. There are 2 such MSX PSC sources, G045.1331+00.1436 and G045.1221+00.1323 (hereafter M1 and M2, respectively; listed in Table 9 and shown in Fig 14). While M1 is close to IR2 ( $\sim 5''$ ), M2 coincides with IR4. From the 2MASS-MSX colour-colour diagram ( $F_{21}/F_8$  vs  $F_8/F_K$ , Lumsden et al. 2002), we find that these sources lie in the region generally covered by compact H II regions. We can, therefore, conclude that these are young stars associated with the cluster.

## 5.2. IRAS 19110+1045

The SED of IRAS 19110+1045 shows a very strong silicate feature at  $10 \mu\text{m}$ . From radiative transfer modelling, we get a higher composition of silicate (60%) grains. The optical depth at  $100 \mu\text{m}$  from the model is obtained to be 0.1. This is consistent with the



value of  $\tau_{100} = 0.085$  obtained by Faison et al. (1998) using their spherically symmetric dust shell model. A gas to dust ratio by mass of 450 is obtained for consistency with radio observations. The dust mass corresponding to the above model is  $450 M_{\odot}$ . On the other hand, the  $130 \mu\text{m}$  emission map gives a dust mass of  $13 M_{\odot}$ . However, based on the sub-millimeter (JCMT-SCUBA) maps, we obtained the cold dust mass to be  $\sim 30 M_{\odot}$  implying a gas mass of  $1.3 \times 10^4 M_{\odot}$ .

From the radio image at 1280 MHz band, we see that this H II region consists of seven radio sources, of which S21-S25 form a complex which is separated from the two compact sources, S26 and S27. This is consistent with what TFT obtained in their high resolution VLA mapping of this source at 4.9 and 8.5 GHz. While S26 and S27 can be identified with TFT11 and TFT12, respectively, TFT30 is resolved into S21-S25. At 610 MHz, these sources are unresolved. The image at 325 MHz shows a single source at this frequency. The ZAMS spectral types as obtained from the radio flux densities from our maps and the maps of TFT are consistent (Table 6).

A comparison of the 1280 MHz radio emission with NIR  $K_s$  band emission is shown in Fig 15. The two compact radio sources, S26 and S27, do not have any NIR counterparts which are detected in all the three JHK<sub>s</sub> bands. We, however, note that there are two sources, designated as K1 and K2, detected only in  $K_s$ -band, which match ( $< 2.5''$ ) with S26 and S27, respectively. It is likely that these objects are deeply embedded. Garay et al. (1986) have used the H76 $\alpha$  line and continuum emission to show that the structure of G45.07+0.13 (positional match with S27) suggests the existence of an ionised ring. According to them, this ionised toroidal structure is likely to correspond to the inner ionised walls of a disk surrounding an inner massive star. This could explain the 2MASS NIR detection only in  $K_s$ -band. Since S26 also has compact radio emission and a NIR counterpart detected only in  $K_s$  band, it is likely that it is also in a similar stage of evolution. Kraemer et al. (2003) have studied this source as a part of their Galactic Ring Survey in the mid infrared ( $12.5 \& 20.6 \mu\text{m}$ ) and they find three mid infrared compact sources, one located at the position of S26 and two close ( $2''$ ) compact sources near S27; the brighter of them matches in position with S27. The OH maser position (Argon et al., 2000) and CO bipolar outflow detected by Hunter et al. (1997) is at the position of S27. Hanson et al. (2002) have reported that this source is heavily reddened in the K band spectrum ( $A_K = 8$ ) and no emission is seen in the H band spectrum.

Considering the radio nebulosity encompassing S21-S25, we find that there are four NIR sources within it. IR8 is very bright in J (8.1) as well as  $K_s$  (6.8) bands. Although lying much higher than the ZAMS curves in the CM diagram, it does not have an associated maser or outflows (as in the case of IR4). It is, therefore, likely to be a foreground source rather than

an embedded early type star associated with this source. We attribute the radio emission to another source, designated K3, detected only in H and  $K_s$  bands. K3 is of ZAMS spectral type O6.5-O6 from the (H-K vs K) CM diagram. The other two sources within the radio nebulosity are of later spectral types (later than B1). Since K3 does not match in position with any of the radio sources, we explore whether S21, ... , S25 are clumps of dense gas externally excited by K3. For this, the role of geometric dilution is considered as discussed for S13 in Section 5.1. We find that only S22 and S24 can barely be excited by K3, while S21, S23 and S25 cannot be ionised by K3.

In this HII region, we find that there are 2 MSX PSC sources, G045.0668+00.1372 and G045.0711+00.1325 (designated M3 & M4, respectively; listed in Table 9 and shown in Fig 15), within the radio nebulosity. M4 is close to K1 and K2 while M3 can be associated with K3. As in the case of IRAS 19111+1048, we obtain the 2MASS-MSX colours ( $F_{21}/F_8$  and  $F_8/F_K$ , Lumsden et al. 2002) and observe that M3 and M4 lie in the general region covered by compact H II regions.

### 5.3. Comparison of properties of IRAS 19111+1048 and IRAS 19110+1045

The properties of the two neighbouring star forming regions as obtained from infrared and radio studies have been compared here. The physical extent of ionised gas around IRAS 19111+1048 (2.8 pc) is larger than its neighbour, IRAS 19110+1045 (1.3 pc). A comparison of optical depth of the cold dust,  $\tau_{100}$ , as obtained from the radiative transfer model indicates that the dust around IRAS 19111+1048 is optically thin ( $\tau_{100} \sim 0.002$ ) compared to that around IRAS 19110+1045 ( $\tau_{100} \sim 0.1$ ). The ratio of total luminosity to the cloud mass of IRAS 19111+1048 and IRAS 19110+1045 are  $170 L_{\odot}/M_{\odot}$  and  $24 L_{\odot}/M_{\odot}$ , respectively. The lower value of  $L/M$  of IRAS 19110+1045 indicates that it is younger than its neighbouring star forming region. The near infrared data as well as high resolution radio measurements indicate that IRAS 19111+1048 has a larger number of ZAMS stars energising compact and evolved H II regions. On the other hand, IRAS 19110+1045 shows the presence of seven radio sources. The NIR counterparts of two of the compact H II sources (S26 and S27) have been detected only in the  $K_s$  band indicating them to be deeply embedded in dust. In view of the above, viz, the lower  $L/M$  ratio of IRAS 19110+1045, its smaller extent of ionised gas, fewer ZAMS stars, the presence of compact H II regions harbouring deeply embedded stars, IRAS 19110+1045 is likely to be younger than IRAS 19111+1048 as suggested by others (Hunter et al. 1997; Kraemer et al. 2003).

## 6. Summary

The star forming regions associated with IRAS 19111+1048 and IRAS 19110+1045 have been studied at infrared (near, mid and far), sub-millimeter as well as low frequency radio wavebands. The dust environment of these regions is probed using data from the TIFR balloon-borne telescope (130 & 200  $\mu\text{m}$ ), MSX, IRAS-HIRES, JCMT-SCUBA and ISO. Using 2MASS PSC, the NIR sources in these regions have been extracted and studied using colour-magnitude (CM) diagrams. The distribution of ionised gas has been obtained using high angular resolution radio maps from GMRT (325, 610 & 1280 MHz). The radio morphology indicates presence of a highly inhomogeneous medium. Twenty compact radio sources have been extracted from IRAS 19111+1048 and seven from IRAS 19110+1045. One of the compact sources (S20) is found to be of non-thermal nature based on its spectral index ( $\alpha = -0.6$ ). The rest of the sources in IRAS 19111+1048 region are of spectral type earlier than B0.5. Based on these sources, the power law index of the initial mass function has been found to be  $5.3 \pm 0.5$  for the mass range  $14 < m/M_{\odot} < 33$ . The compact source, S14, is located at the position of this IRAS source. The near infrared (NIR) source coincident with the IRAS peak is likely to be an embedded pre-main sequence star due to its large infrared excess as well as the presence of OH maser and CO bipolar outflow here. The electron temperature and emission measure of S14 using results from GMRT (our work) and VLA (TFT) measurements are determined to be  $8346 \pm 1511$  K and  $8.8 \pm 0.7 \times 10^6$   $\text{cm}^{-6}\text{pc}$ , respectively. A comparison of NIR and radio images has been carried out to identify the exciting sources and their nature. The spectral types determined from NIR and radio measurements are found to match very well for a good fraction of radio sources having NIR counterparts. The radio and infrared morphology of IRAS 19110+1045 indicates that the extent of dust as well ionised gas is relatively smaller than that of IRAS 19111+1048. The two compact radio sources, S26 and S27, have been detected only in the  $K_s$ -band, indicating these to be deeply embedded. Self-consistent radiative transfer modelling has been carried out through spherical gas-dust clouds for both the IRAS sources, using a cluster of OB stars as determined from the radio maps. A constant radial density distribution ( $n(r) \propto r^0$ ) is preferred. The geometric details of the gas-dust clouds, the dust composition and optical depths etc. have been quantified by the models. A comparative study of the infrared and radio properties of IRAS 19110+1045 and IRAS 19111+1048 support the younger nature of the former, consistent with earlier studies.

We thank the anonymous referee for comments and suggestions which improved the paper. It is a pleasure to thank several members of the Infrared Astronomy Group of TIFR for their support during the balloon flight campaigns. All members of the TIFR Balloon Facility, Hyderabad, are thanked for their technical support for the flight. We thank the

staff of the GMRT who have made the radio observations possible. GMRT is run by the National Centre for Radio Astrophysics of the Tata Institute of Fundamental Research. We thank IPAC, Caltech, for providing us the HIRES-processed IRAS products.

## REFERENCES

- Altenhoff, W. J., Downes, D., Pauls, T. & Schraml, J. 1979, *A&AS*, 35, 23
- Araya, E., Hofner, P., Churchwell, E. & Kurtz, S. 2002, *ApJS*, 138, 63
- Argon, A. L., Reid, M. J. & Menten, K. M. 2000, *ApJS*, 129, 159
- Aumann, H. H., Fowler, J. W. & Melnyk, M. 1990, *AJ*, 99, 1674
- Bessel, M. S. & Brett, J. M. 1988, *PASP*, 100, 1134
- Clegg, P. E., Ade, P. A. R., Armund, C. et al. 1996, *A&A*, 315, L38
- Darbon, S., Zavagno, A., Perrin, J. -M, Savine, C., Ducci, V. & Sivan, J., -P. 2000, *A&A*, 364, 723
- de Graauw, Th., Haser, L. N., Beintema, D. A, et al. 1996, *A&A*, 315, L49
- Draine, B. T. & Lee, H. M. 1984, *ApJ*, 285, 89
- Egan, M. P., Price, S. D., Kraemer, et al. 2003, Air Force Research Laboratory Technical Report, AFRL-VS-TR-2003-1589
- Faison, M., Churchwell, E., Hofner, P., Hackwell, J., Lynch, D. K. & Russell, R. W. 1998, *ApJ*, 500, 280
- Fish, V. L., Reid, M. J., Wilner, D. J. & Churchwell, E. 2003, *ApJ*, 587, 701
- Frieswijk, W. F., Shipman, R. F. & Lahuis, F. 2004, ISO Technical Note 12
- Garay, G., Rodriguez, L. F. & van Gorkom, J. H. 1986, *ApJ*, 309, 553
- Genzel, R. & Downes, D. 1977, *A&AS*, 30, 145
- Ghosh, S. K., Iyengar, K. V. K., Rengarajan, S. N., Tandon, S. N., Verma, R. P. & Daniel, R. R. 1988, *ApJ*, 330, 928
- Ghosh, S. K., Iyengar, K. V. K., Rengarajan, T. N., Tandon, S. N., Verma, R. P., Daniel, R. R. & Ho, P. T. P. 1989, *ApJ*, 347, 338

- Ghosh, S. K. & Ojha, D. K. 2002, *A&A*, 288, 326
- Goss, W. M., Lockhart, I. A., Fomalont, E. B. & Hardebeck, E. G. 1973, *ApJ*, 183, 843
- Gull, S. F. & Daniell, G. J. 1978, *Nature*, 272, 686
- Hanson, M. M., Luhman, K. L. & Rieke, G. H. 2002, *ApJS*, 138, 35
- Haslam, C. G. T., Stoffel, H., Salter, C. J. & Wilson, W. E. 1982, *A&AS*, 47, 1
- Hildebrand, R. H. 1983, *QJRAS*, 24, 267
- Hoare, M. G., Roche, P. F. & Glencross, W. M. 1991, *MNRAS*, 251, 584
- Hunter, T. R., Phillips, T. G. & Menten, K. M. 1997, *ApJ*, 478, 283
- IRAS Science Team, 1986, *A&AS*, 65, 607
- Israel, F. P. 1982, *ApJ*, 255, 475
- Kraemer, K. E., Jackson, J. M., Kassis, M., et al. 2003, *ApJ*, 588, 918
- Lloyd, C., Lerate, M. R. & Grundy, T. W., 2003, *ISO Technical Note 17*
- Lumsden, S. L. & Puxley, P. J. 1996, *MNRAS*, 281, 493
- Lumsden, S. L., Hoare, M. G., Oudmaijer, R. D. & Richards, D. 2002, *MNRAS*, 336, 621
- Mathis, J. S., Mezger, P. G. & Panagia, N. 1983, *A&A*, 128, 212
- Matthews, H. E., Goss, W. M., Winnberg, A. & Habing, H. J. 1977, *A&A*, 61, 261
- Mezger, P. G. & Henderson, A. P. 1967, *ApJ*, 147, 471
- Mookerjea, B. & Ghosh, S. K. 1999, *J. Astrophys. Astr.* 20, 1
- Naik, M. V., D'Costa, S. L., Ghosh, S. K., Mookerjea, B., Ojha, D. K. & Verma, R. P. 2000, *Publ. Astron. Soc. Pac.*, 112, 273
- Ojha, D. K., Ghosh, S. K., Kulkarni, V. K., Testi, L., Verma, R. P. & Vig, S. 2004a, *A&A*, 415, 1039
- Ojha, D. K., Tamura, M., Nakajima, Y., et al. 2004b, *ApJ*, 616, 1042
- Panagia, N. 1973, 78, 929
- Pankonin, V., Churchwell, E., Watson, C. & Bieging, J. H. 2001, *ApJ*, 558, 194

- Price, S. D., Egan, M. P., Carey, S. J., Mizuno, D. R., & Kuchar, T. A. 2001, *AJ*, 121, 2819
- Rieke, G. H. & Lebofsky, M. J. 1985, *ApJ*, 288, 618
- Sandell, G. 2000, *A&A*, 358, 242
- Sanders, D. B., Clemens, D. B., Scoville, N. Z. & Solomon, P. M. 1986, *ApJS*, 60, 1
- Simon, R., Jackson, J. M., Clemens, D. P. & Bania, T. M. 2001, *ApJ*, 551, 747
- Schraml, J. & Mezger, P. G. 1969, *ApJ*, 156, 269
- Shepherd, D. 2005, *Astro-ph* 0506024
- Sloan, G. C., Kraemer, K. E., Price, S. D. & Shipman, R. F. 2003, *ApJS*, 147, 379
- Swarup, G., Ananthakrishnan, S., Kapahi, V. K., Rao, A. P., Subrahmanya, C. R., & Kulkarni, V. K., 1991, *Current Science*, 60, 95
- Testi, L., Felli, M. & Taylor, G. B. 1999, *A&AS*, 138, 71 (TFT)
- Wood, D. O. S. & Churchwell, E. 1989, 69, 831

Table 1: Details of the radio continuum observations carried out using the Giant Metrewave Radio Telescope (GMRT), India.

Frequency band (MHz)	1280	610	325
Date of Observation	28 Oct 2001	06 Jan 2002	30/31 Aug 2002
Primary beam	21'.6	54'	1°.8
Synthesized beam	7".5 × 3".8	8".4 × 6".6	14".4 × 11".5
Position angle	-34°.4	-73°.8	68°.4
Map noise (mJy/beam)	0.8	0.7	1.3
Continuum bandwidth	16 MHz	16 MHz	16 MHz

Table 2: Flux density details of IRAS 19111+1048 and IRAS 19110+1045.

IRAS PSC	Flux Density (Jy) for $\lambda$ ( $\mu\text{m}$ )									
	TIFR images <sup>a</sup>		IRAS-HIRES images <sup>a</sup>				MSX images <sup>a</sup>			
Source			IRAS PSC							
	200	130	100	60	25	12	21.3	14.7	12.1	8.3
19111+1048	1145	2889	6054	7024	1607	320	1411	511	316	119
			7497	5913	1395	250				
19110+1045	-	2261	4409	4311	567	72.0	319	125	66	32
			< 7497	< 5913	494	58				

<sup>a</sup> Fluxes obtained by integrating over a circular region of diameter 3' centered on the peak.

Table 3: List of extracted sources along with their peak and integrated flux densities obtained from the radio maps of IRAS 19111+1048.

Source No.	RA (2000) h m s	Dec (2000) ° ' "	1280 MHz		610 MHz	
			Peak flux mJy/bm	Int flux mJy	Peak flux mJy/bm	Int flux mJy
S1	19 13 23.0	+10 54 20	16.5 ± 0.5	77.0 ± 2.7	–	–
S2	19 13 24.0	+10 53 42	20.5 ± 0.5	117.5 ± 3.5	–	–
S3	19 13 24.7	+10 54 01	22.4 ± 0.5	81.5 ± 2.4	–	–
S4	19 13 24.7	+10 54 19	28.0 ± 0.5	169.2 ± 3.7	19.6 ± 0.7	115.2 ± 5.2
S5	19 13 24.9	+10 54 41	23.5 ± 0.5	90.2 ± 2.2	–	–
S6	19 13 24.9	+10 53 48	34.5 ± 0.5	325.5 ± 5.5	22.5 ± 0.6	313.6 ± 7.5
S7	19 13 25.7	+10 54 00	56.4 ± 0.5	256.7 ± 2.9	25.6 ± 0.7	221.8 ± 9.2
S8	19 13 25.8	+10 54 24	67.3 ± 0.5	328.1 ± 3.0	–	–
S9	19 13 26.1	+10 54 12	44.8 ± 0.5	247.1 ± 3.4	–	–
S10	19 13 26.1	+10 54 02	37.4 ± 0.5	157.3 ± 2.7	–	–
S11	19 13 26.9	+10 54 29	101.3 ± 0.5	1261.7 ± 6.3	–	–
S12	19 13 26.9	+10 54 17	88.3 ± 0.5	669.6 ± 4.5	–	–
S13	19 13 27.5	+10 54 03	21.7 ± 0.5	103.7 ± 3.0	–	–
S14	19 13 27.8	+10 53 36	487.8 ± 0.5	2156.6 ± 2.8	150.7 ± 0.8	833.7 ± 5.1
S15	19 13 28.1	+10 54 18	27.9 ± 0.5	136.3 ± 3.0	–	–
S16	19 13 28.4	+10 54 06	26.3 ± 0.5	97.9 ± 2.5	–	–
S17	19 13 28.5	+10 53 44	18.1 ± 0.5	53.7 ± 2.1	–	–
S18	19 13 28.7	+10 54 13	20.0 ± 0.5	97.4 ± 2.9	30.0 ± 0.8	89.3 ± 3.0
S19	19 13 28.8	+10 53 55	72.4 ± 0.5	178.7 ± 2.0	43.5 ± 0.8	154.7 ± 3.5
S20 <sup>a</sup>	19 13 29.7	+10 53 58	20.0 ± 0.5	21.1 ± 1.0	29.4 ± 0.9	30.6 ± 1.6

<sup>a</sup> Non-thermal source



Table 4: List of extracted sources along with their peak and integrated flux densities obtained from the radio map of IRAS 19110+1045.

Source No.	RA (2000) h m s	Dec (2000) ° ' "	1280 MHz		610 MHz	
			Peak flux mJy/bm	Int flux mJy	Peak flux mJy/bm	Int flux mJy
S21	19 13 19.4	10 50 51	$27.1 \pm 0.6$	$124.1 \pm 2.2$	–	$426.1^a \pm 4.0$
S22	19 13 20.1	10 50 48	$45.9 \pm 0.6$	$183.3 \pm 2.2$	–	$426.1^a \pm 4.0$
S23	19 13 20.3	10 50 59	$32.4 \pm 0.6$	$87.5 \pm 1.8$	–	$426.1^a \pm 4.0$
S24	19 13 20.4	10 50 49	$42.9 \pm 0.4$	$81.9 \pm 1.4$	–	$426.1^a \pm 4.0$
S25	19 13 20.8	10 50 59	$23.2 \pm 0.6$	$28.0 \pm 1.0$	–	$426.1^a \pm 4.0$
S26	19 13 21.7	+10 50 48	$56.0 \pm 0.6$	$69.5 \pm 1.3$	–	$34.9^b \pm 1.3$
S27	19 13 22.0	+10 50 52	$30.6 \pm 0.6$	$44.5 \pm 1.4$	–	$34.9^b \pm 1.3$

<sup>a</sup> Same value of integral flux density is given as S21 - S25 are unresolved

<sup>b</sup> Same value of integral flux density is given as S26 & S27 are unresolved

Table 5: List of radio (GMRT and VLA) and near infrared sources along with their spectral types around IRAS 19111+1048.

Radio (GMRT)		Radio (VLA) <sup>a</sup>		NIR (2MASS)	
Name	Spec type	Name	Spec type	Name	Spec type
S1	B0-O9.5	-	-	-	-
S2	B0-O9.5	-	-	-	-
S3	B0-O9.5	-	-	-	-
S4	B0-O9.5	-	-	-	-
S5	B0-O9.5	-	-	-	-
S6	O9	TFT13	O9.5	IR1	B0-O9
S7	O9.5-O9	-	-	-	-
S8	O9	-	-	-	-
S9	O9.5-O9	-	-	-	-
S10	B0-O9.5	-	-	-	-
S11	O7	-	-	IR2	O9-O6
S12	O8	-	-	IR3	B2
S13	B0.5-B0	-	-	-	-
S14	O6.5-O6	TFT15	O6	IR4, IR5	X <sup>b</sup> , O5
S15	B0-O9.5	-	-	-	-
S16	B0.5-B0	-	-	IR6	B7-B3
S17	B0.5-B0	-	-	-	-
S18	B0-O9.5	TFT16	B0-O9.5	-	-
S19	B0-O9.5	TFT17	B0-O9.5	IR7	B7-B3

<sup>a</sup> Work of Testi, Felli & Taylor (1999)

<sup>b</sup> Either a pre-main sequence star or compact unresolved stars (see Section 5)

Table 6: List of radio (GMRT and VLA) and near infrared sources along with their spectral types around IRAS 19110+1045 region.

Radio (GMRT)		Radio (VLA) <sup>a</sup>		NIR (2MASS)	
Name	Spec type	Name	Spec type	Name	Spec type
S21	B0-O9.5	-	-	-	-
S22 <sup>b</sup>	B0-O9.5	-	-	K3	O6.5-O6
S23 <sup>b</sup>	B0-O9.5	-	-	K3	O6.5-O6
S24	B0-O9.5	-	-	-	-
S25	B0.5-B0	-	-	-	-
S26	B0-O9.5	TFT11	O9.5-O8.5	K1	-
S27	B0.5-B0	TFT12	B0-O9.5	K2	-

<sup>a</sup> Work of Testi, Felli & Taylor (1999)

<sup>b</sup> Radio knots which could be thermally excited by K3.

Table 7: Details of 2MASS PSC sources which are likely to be associated with GMRT sources at 1280 MHz (see Tables 5 and 6) in IRAS 19111+1048 and IRAS 19110+1045 regions.

2MASS PSC designation	Name <sup>a</sup>	$\alpha_{2000}$ (deg)	$\delta_{2000}$ (deg)	J (mag)	H (mag)	$K_s$ (mag)
IRAS 19111+1048						
J19132485+1053474	IR1	288.353577	10.896520	$14.64 \pm 0.04$	$13.11 \pm 0.04$	$12.35 \pm 0.05$
J19132689+1054176	IR3	288.362067	10.904891	$15.23 \pm 0.13$	$14.14 \pm 0.13$	$12.83 \pm 0.12$
J19132692+1054269	IR2	288.362188	10.907485	$13.10 \pm 0.03$	$12.03 \pm 0.04$	$11.50 \pm 0.04$
J19132786+1053364	IR4	288.366123	10.893447	$11.87 \pm 0.03$	$9.97 \pm 0.04$	$7.85 \pm 0.03$
J19132812+1053297	IR5	288.367173	10.891603	$13.76 \pm 0.06$	$11.98 \pm 0.07$	$10.08 \pm 0.05$
J19132823+1054056	IR6	288.367652	10.901567	$16.35 \pm 0.14$	$15.21 \pm 0.09$	$14.95 \pm 0.20$
J19132895+1053560	IR7	288.370642	10.898909	$15.88 \pm 0.09$	$14.96 \pm 0.09$	$13.58 \pm 0.10$
IRAS 19110+1045						
J19131970+1050478	IR8	288.332099	10.846624	$8.14 \pm 0.01$	$7.23 \pm 0.03$	$6.83 \pm 0.02$
J19132008+1050527	K3	288.333708	10.847999	–	$12.55 \pm 0.19$	$11.52 \pm 0.09$
J19132184+1050484	K1	288.341025	10.846782	–	–	$13.14 \pm 0.14$
J19132208+1050538	K2	288.342034	10.848284	–	–	$10.54 \pm 0.03$

<sup>a</sup> Short name used in the present work (see figures 11, 14 and 15)

Table 8: Best-fit parameters of the radiative transfer models for IRAS 19111+1048 and IRAS 19110+1045.

Source	$\alpha$	$R_{max}$	$R_{min}$	$r_{HII}$	$\tau_{100}$	L	Dust	Composition	$M_{dust}$	Gas:Dust
IRAS		(pc)	(pc)	(pc)		( $10^5 L_{\odot}$ )	Type	Si:C	( $M_{\odot}$ )	
19111+1048	0.0	4.0	0.01	1.5	0.002	8.5	DL	5:95	12	250:1
19110+1045	0.0	3.5	0.01	0.04	0.10	3.3	DL	60:40	450	450:1

Table 9: Details of the MSX PSC sources within the radio nebulosity of IRAS 19111+1048 and IRAS 19110+1045 regions.

MSX PSC designation	Name <sup>a</sup>	$\alpha_{2000}$ (deg)	$\delta_{2000}$ (deg)	$F_8$ (Jy)	$F_{12}$ (Jy)	$F_{14}$ (Jy)	$F_{21}$ (Jy)
G045.1331+00.1436	M1	288.3610	10.9083	$4.7 \pm 0.2$	$8.3 \pm 0.9$	$32.1 \pm 2.0$	$57.6 \pm 3.5$
G045.1221+00.1323	M2	288.3660	10.8933	$87.5 \pm 3.6$	$296.4 \pm 14.8$	$455.7 \pm 27.8$	$1061.7 \pm 63.7$
G045.0711+00.1325	M3	288.3417	10.8482	$20.3 \pm 0.8$	$53.8 \pm 2.7$	$119.3 \pm 7.3$	$256.0 \pm 15.4$
G045.0668+00.1372	M4	288.3354	10.8466	$3.6 \pm 0.1$	$9.0 \pm 0.5$	$11.0 \pm 0.7$	$35.8 \pm 2.2$

<sup>a</sup> Short name used in the present work (see figures 14 and 15)

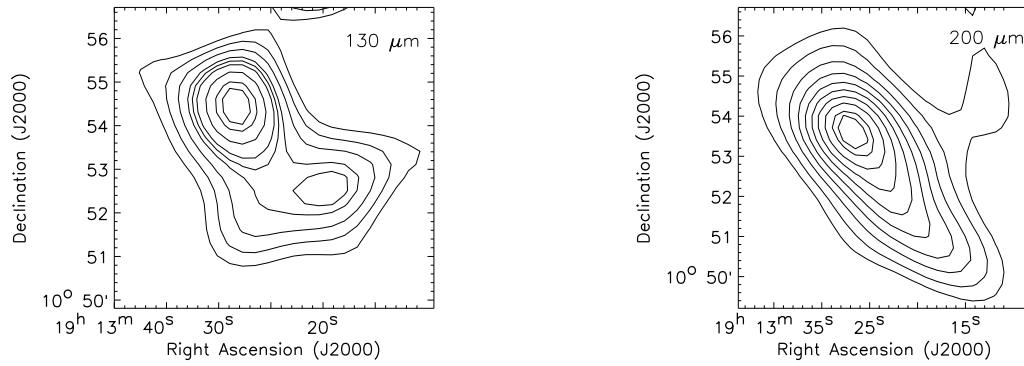


Fig. 1.— The intensity map for the region around IRAS 19111+1048 which includes IRAS 19110+1045 at  $130 \mu\text{m}$  (left) and  $200 \mu\text{m}$  (right). The effective beamsize for these observations is  $\sim 1'.7$ . (Left) Contour levels are at 30, 40, 50, 60, 65, 70, 80, 90, 95% of peak intensity of  $620 \text{ Jy arcmin}^{-2}$ . (Right) Contour levels are at 12, 20, 30, 40, 50, 60, 70, 80, 90, 95% of peak intensity of  $261 \text{ Jy arcmin}^{-2}$ .

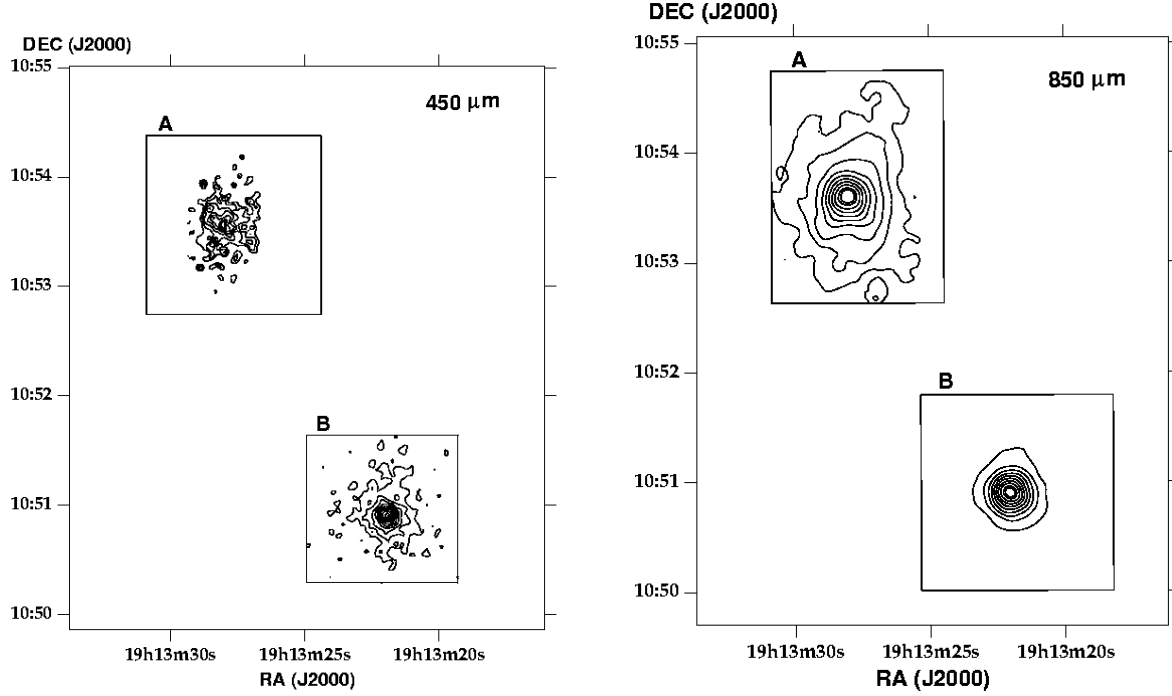


Fig. 2.— Spatial distribution of cold dust emission as obtained from JCMT at  $450\ \mu\text{m}$  (left) and  $850\ \mu\text{m}$  (right) around the region IRAS 19111+1048 (A) and IRAS 19110+1045 (B). The contour levels of A are at 40, 50, 60, 70, 80, 90, 95 % of peak value of  $25.5\ \text{Jy/beam}$  at  $450\ \mu\text{m}$  and 10, 20, 30, 40, 50, 60, 70, 80, 90, 95 % of the peak value of  $6.9\ \text{Jy/beam}$  at  $850\ \mu\text{m}$ . For B, the contour levels are at 10, 20, 30, 40, 50, 60, 70, 80, 90, 95 % of the peak values of  $161.4\ \text{Jy/beam}$  and  $11.0\ \text{Jy/beam}$  at  $450\ \mu\text{m}$  &  $850\ \mu\text{m}$ , respectively. The maps at  $450\ \mu\text{m}$  (left) have a beam size of  $\sim 7'' \times 11''$  and at  $850\ \mu\text{m}$  (right) have a beam size of  $\sim 13'' \times 17''$ .

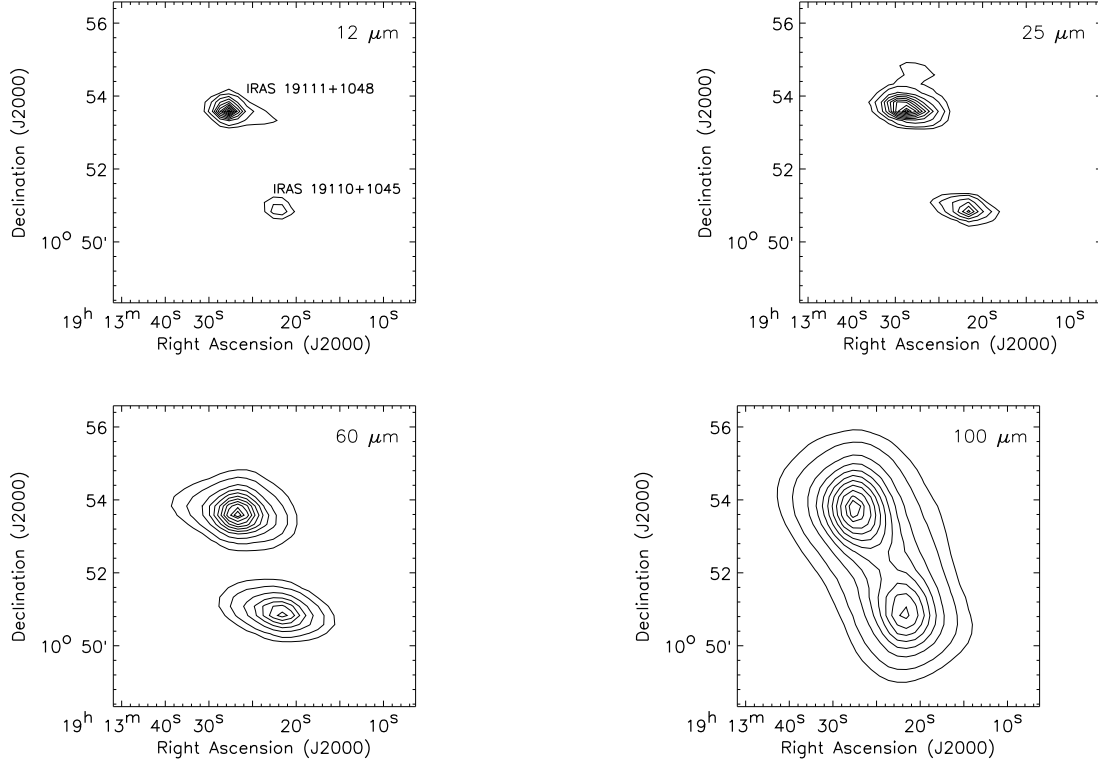


Fig. 3.— The IRAS-HIRES intensity maps for the region covering IRAS 19111+1048 and IRAS 19110+1045 at 12  $\mu\text{m}$  (top left), 25  $\mu\text{m}$  (top right), 60  $\mu\text{m}$  (bottom left) and 100  $\mu\text{m}$  (bottom right). The size of the beams are  $0'.75 \times 4'.5$  at 12  $\mu\text{m}$ ,  $0'.75 \times 4'.6$  at 25 $\mu\text{m}$ ,  $1'.5 \times 4'.7$  at 60  $\mu\text{m}$  and  $3'.0 \times 5'.0$  at 100  $\mu\text{m}$ . However, the achieved angular resolution of these HIREs maps are much higher (see text). The contours are at 5, 10, 20, 30, 40, 50, 60, 70, 80, 90 and 95 % of the peak value of 939 Jy arcmin<sup>-2</sup>, 2350 Jy arcmin<sup>-2</sup>, 5100 Jy arcmin<sup>-2</sup> and 1970 Jy arcmin<sup>-2</sup> at 12, 25, 60 and 100  $\mu\text{m}$ , respectively.



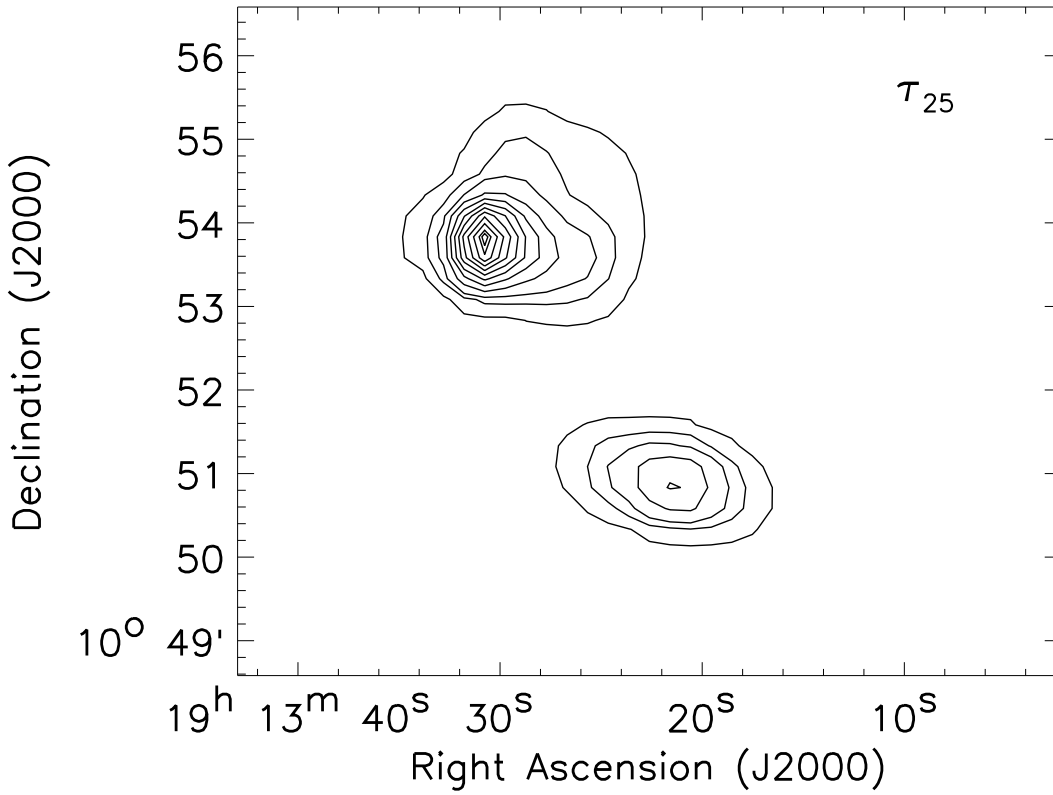


Fig. 4.— The distribution of optical depth at 25  $\mu\text{m}$ ,  $\tau_{25}$ , of the region around IRAS 19111+1048 and IRAS 19110+1045 assuming a dust emissivity law of  $\epsilon_\lambda \propto \lambda^{-1}$ . The  $\tau_{25}$  contours represent 1, 5, 10, 20, 30, 40, 50, 60, 70, 80 and 90 % of the peak value of 0.001.

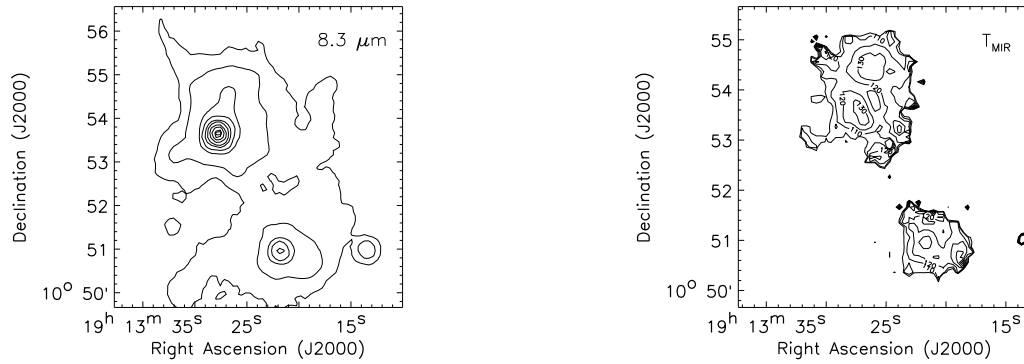


Fig. 5.— The spatial distribution of continuum emission in the MSX 8.3  $\mu\text{m}$  band (left) with beam  $\sim 18''$  and mid-infrared temperature,  $T_{\text{MIR}}$  (right). The contour levels are at (left) 0.1, 0.5, 1, 5, 10, 20, 30, 40, 50, 60, 70, 80, 90, 95 % of peak value of  $473.7 \text{ Jy arcmin}^{-2}$  and (right) 100, 110, 120, 130, 140, 150 and 160 K.

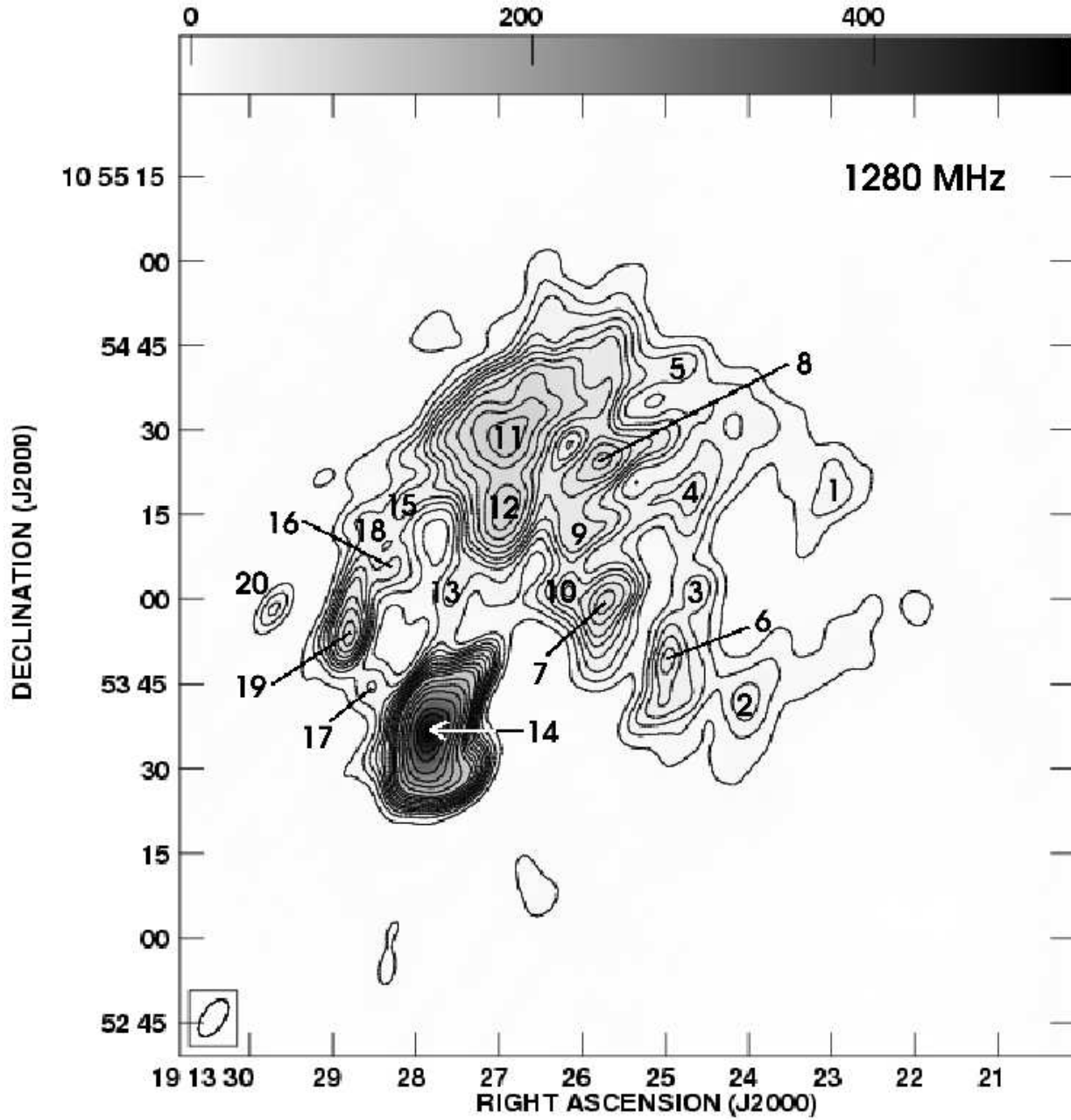


Fig. 6.— Radio continuum emission at 1280 MHz from IRAS 19111+1048. The contour levels are at  $3.0 \times (-2, 2, 4, 6, 8, 10, 12, 15, 18, 22, 26, 31, 42, 54, 70, 90, 120, 140)$  mJy/beam. The beam size is  $7''.5 \times 3''.8$  and rms noise in the map is  $\sim 0.8$  mJy/beam. The discrete radio sources are represented by the numbers as listed in Tables 3 and 5.

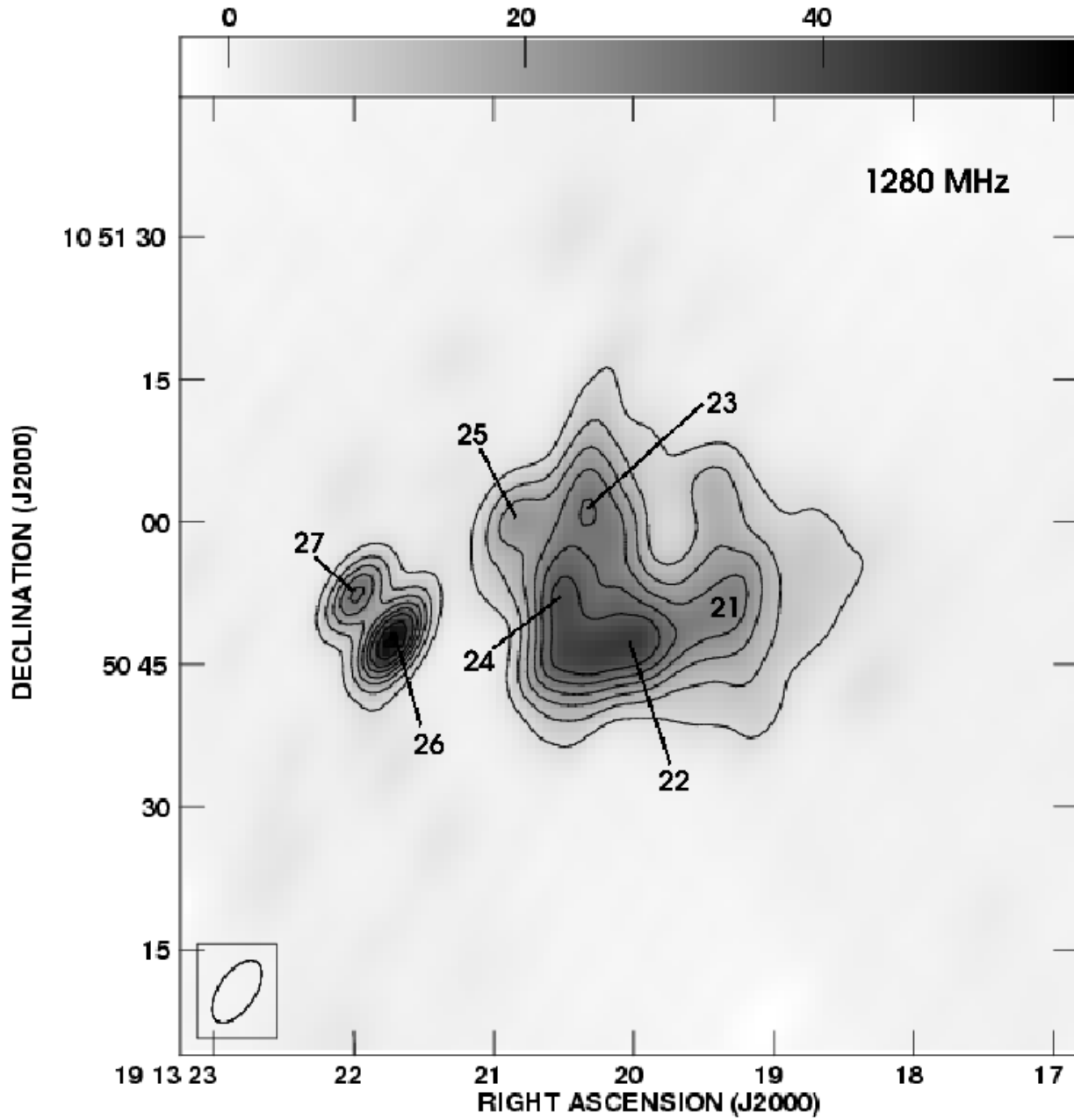


Fig. 7.— Radio continuum emission at 1280 MHz from IRAS 19110+1045. The contours are at levels  $3.0 \times (-2, 2, 4, 6, 8, 10, 12, 14, 16, 18)$  mJy/beam. The beam size is  $7''.5 \times 3''.8$  and rms noise in the map is  $\sim 0.8$  mJy/beam. The discrete radio sources are represented by the numbers as listed in Tables 4 and 6.

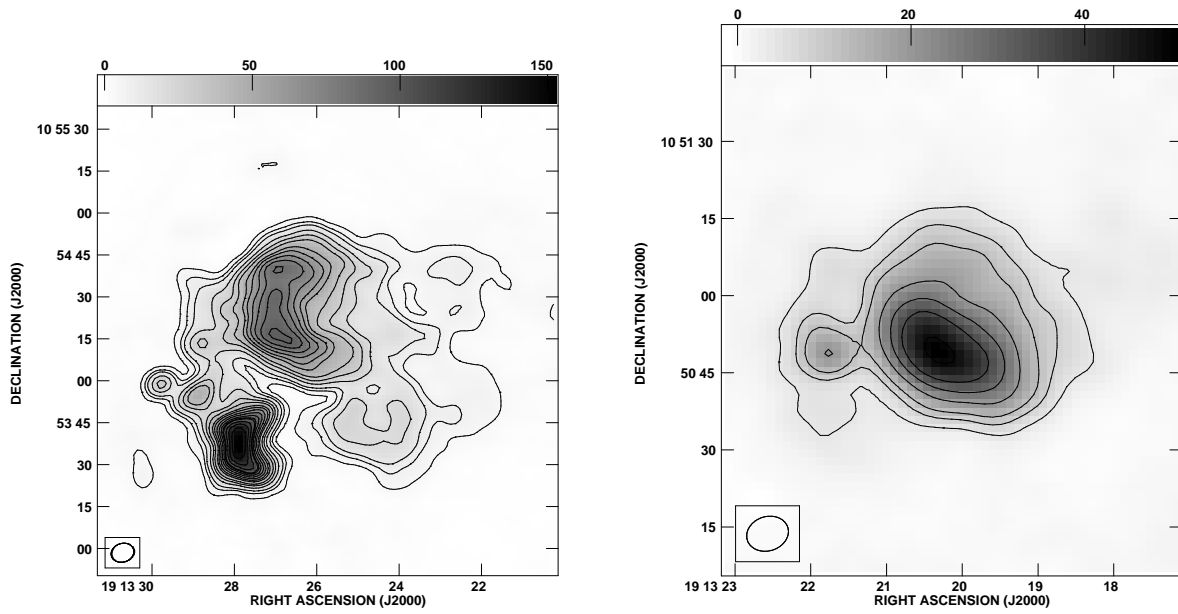


Fig. 8.— Radio continuum emission at 610 MHz from IRAS 19111+1048 (left) and IRAS 19110+1045 (right). The contour levels are at (left)  $2.0 \times (-2, 2, 4, 6, 10, 14, 18, 24, 28, 33, 38, 43, 47, 49, 55, 61, 68, 75, 82)$  mJy/beam and (right)  $2.0 \times (-2, 2, 4, 6, 10, 14, 18, 24)$  mJy/beam. The beam size is  $8''.2 \times 6''.6$  and the rms noise in the map is  $\sim 0.7$  mJy/beam.

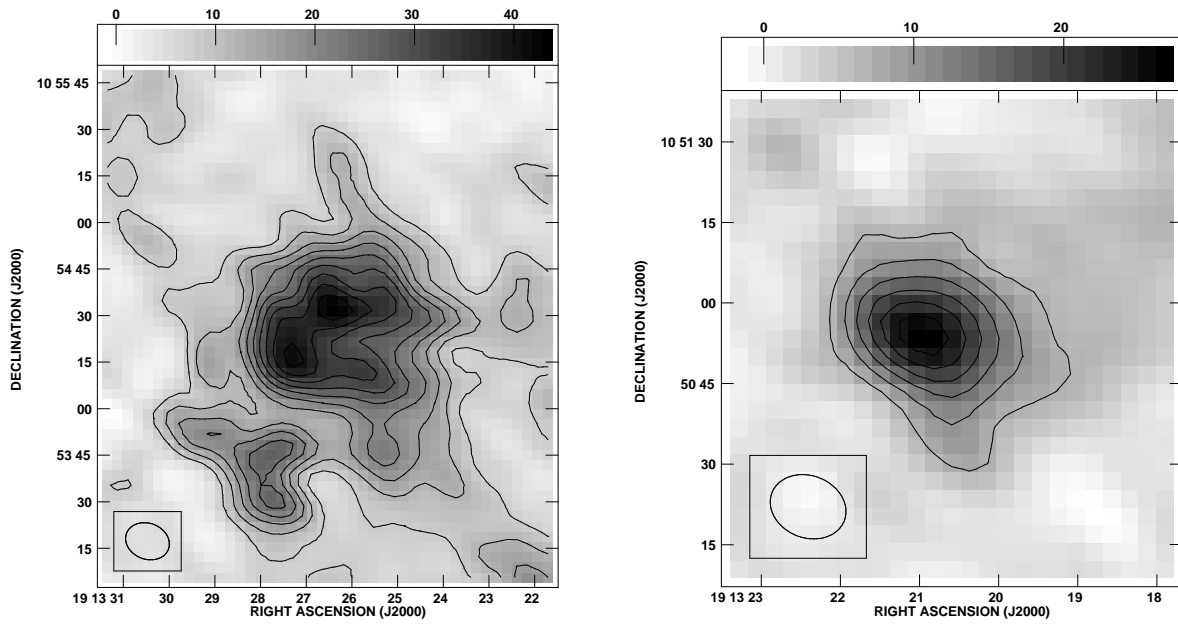


Fig. 9.— Radio continuum emission at 325 MHz from IRAS 19111+1048 (left) and IRAS 19110+1045 (right). The contour levels are at (left)  $4.0 \times (-2, 2, 3, 4, 5, 6, 7, 8, 9, 10)$  mJy/beam and (right)  $3.5 \times (-2, 2, 3, 4, 5, 6, 7)$  mJy/beam. The beam size is  $14''.5 \times 11''.4$  and map noise is  $\sim 1.3$  mJy/beam.

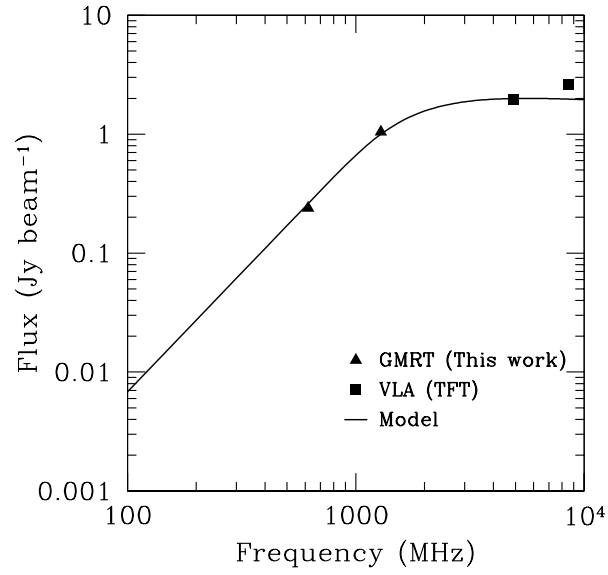


Fig. 10.— The observed (triangles and squares represent GMRT & VLA measurements, respectively) and modelled (line) flux densities for the core of the H II region, S14, in IRAS 19111+1048. The flux densities correspond to a beam size of 10".

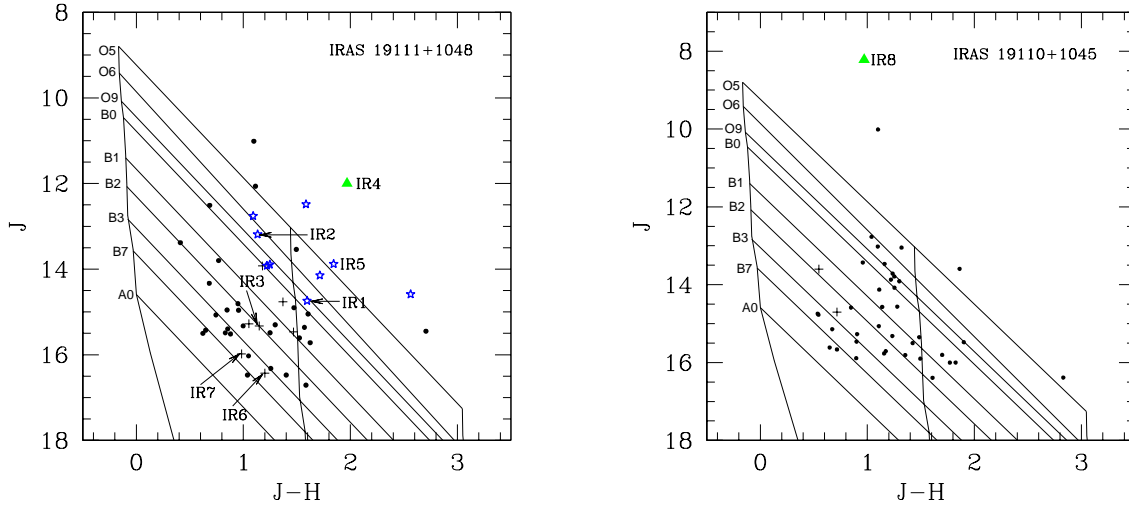


Fig. 11.— Color-magnitude diagram ( $J-H$  vs  $J$ ) for sources detected in all the 2MASS three bands for region around IRAS 19111+1048 (left) and IRAS 19110+1045 (right). The nearly vertical solid lines from left to right represent the zero age main sequence (ZAMS) curves reddened by  $A_V = 0, 15$  and  $30$  mag, respectively. The slanting lines trace the reddening vectors of these ZAMS stars. The asterisk symbols represent stars of spectral type B0 or earlier. The triangle represents an embedded source, possibly in its very early evolutionary stage or unresolved early type stars. The plus symbols are sources of spectral type later than B0 within the radio nebulosity. The dot symbols represent selected sources not lying within the radio nebulosity.



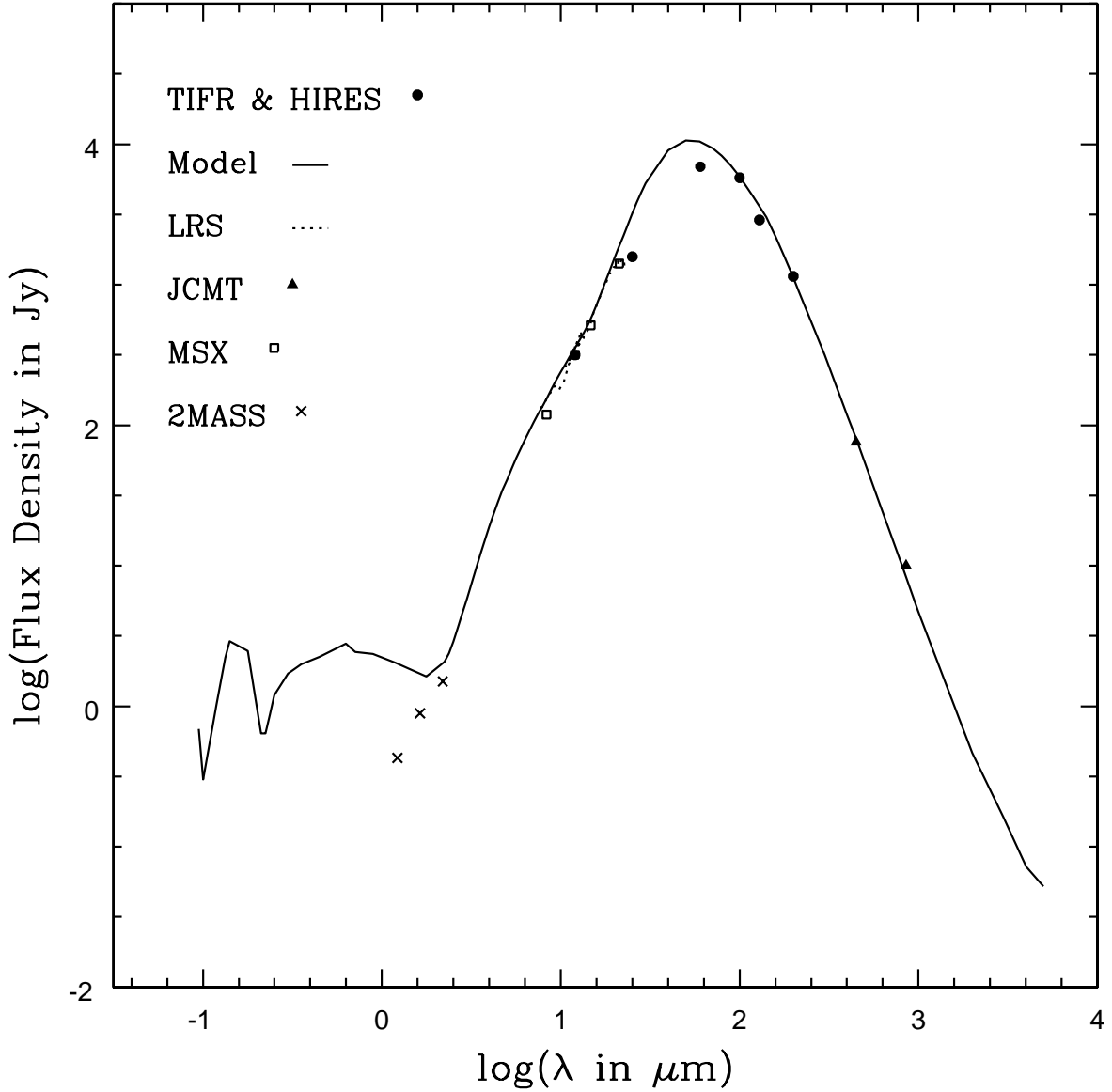


Fig. 12.— Comparison of the spectral energy distribution from observations and the best fit radiative transfer model of IRAS 19111+1048. The filled circles represent the TIFR and IRAS-HIRES data. The dashed lines are the IRAS-LRS spectra. The filled triangles denote JCMT data while the open squares represent the MSX data. The 2MASS data is denoted by cross-symbols. The solid line denotes the best fit model to the data. See text and Table 8 for details of model parameters.

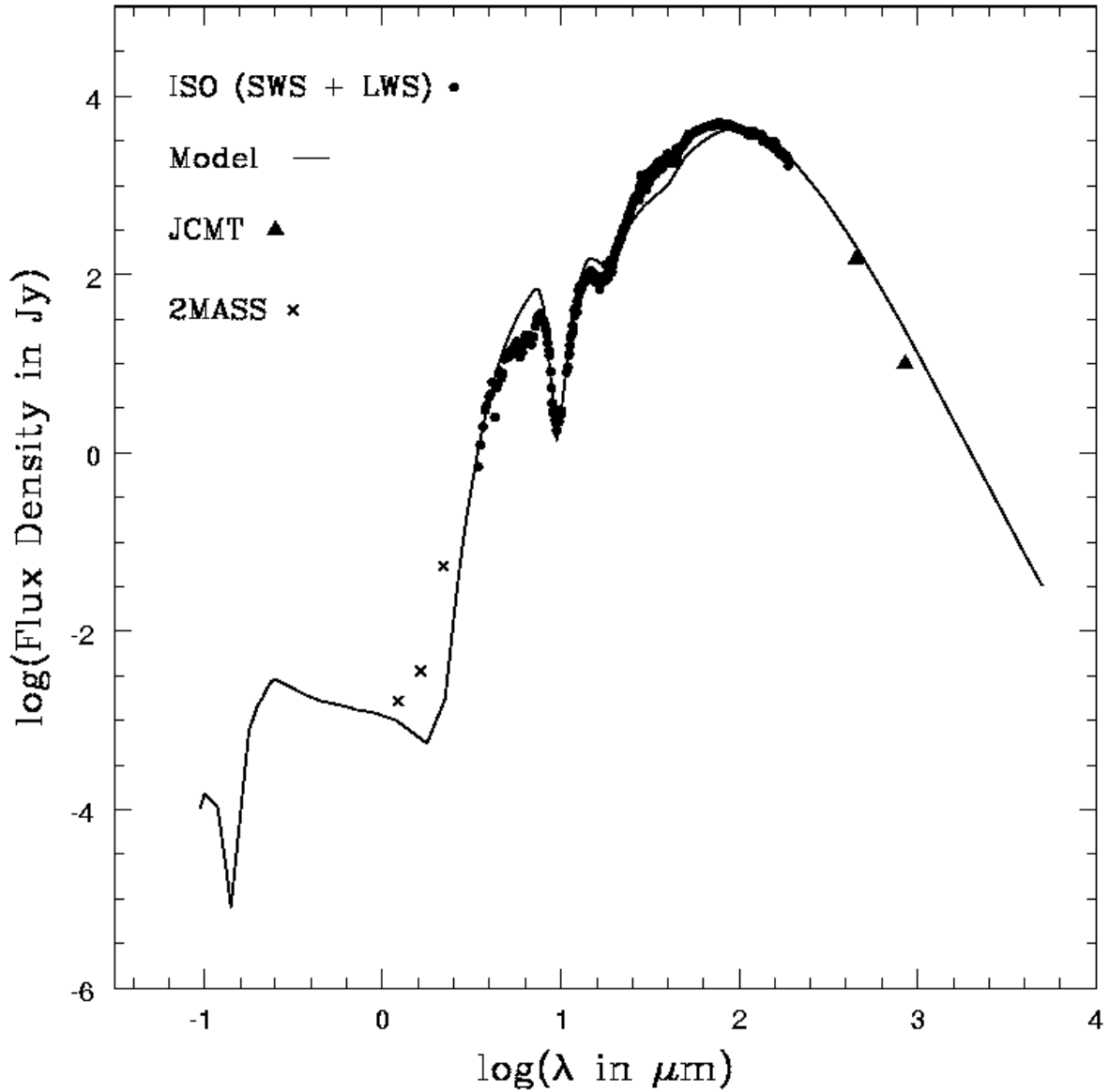


Fig. 13.— Comparison of the spectral energy distribution from observations and the best fit radiative transfer model of IRAS 19110+1045 for ISO data. The filled circles represent the ISO SWS and LWS data, the filled triangles represent JCMT data and the crosses represent the 2MASS data. The solid line denotes the best fit model to the data. See Table 8 for details of model parameters.

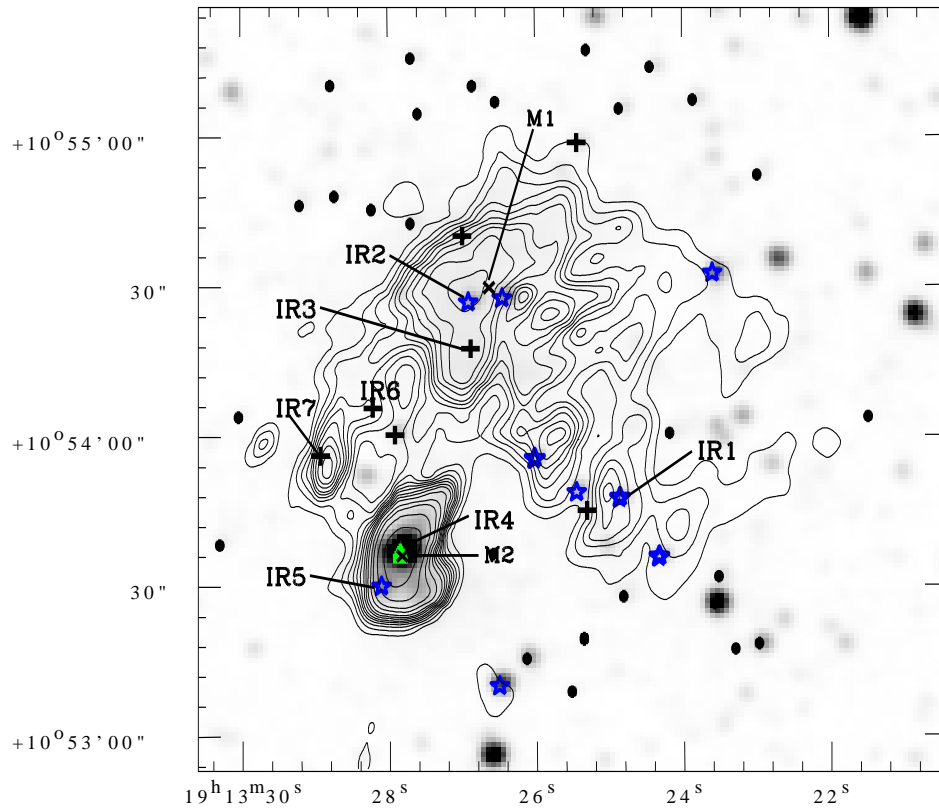


Fig. 14.— Contours of high resolution radio continuum emission at 1280 MHz overlaid over grayscale 2MASS  $K_s$ -band image for the region around IRAS 19111+1048. The labelled axes are in J2000 coordinates. Various NIR and MSX sources are marked. The cross-symbols represent MSX sources. The description of the other symbols is the same as given in Fig 11.

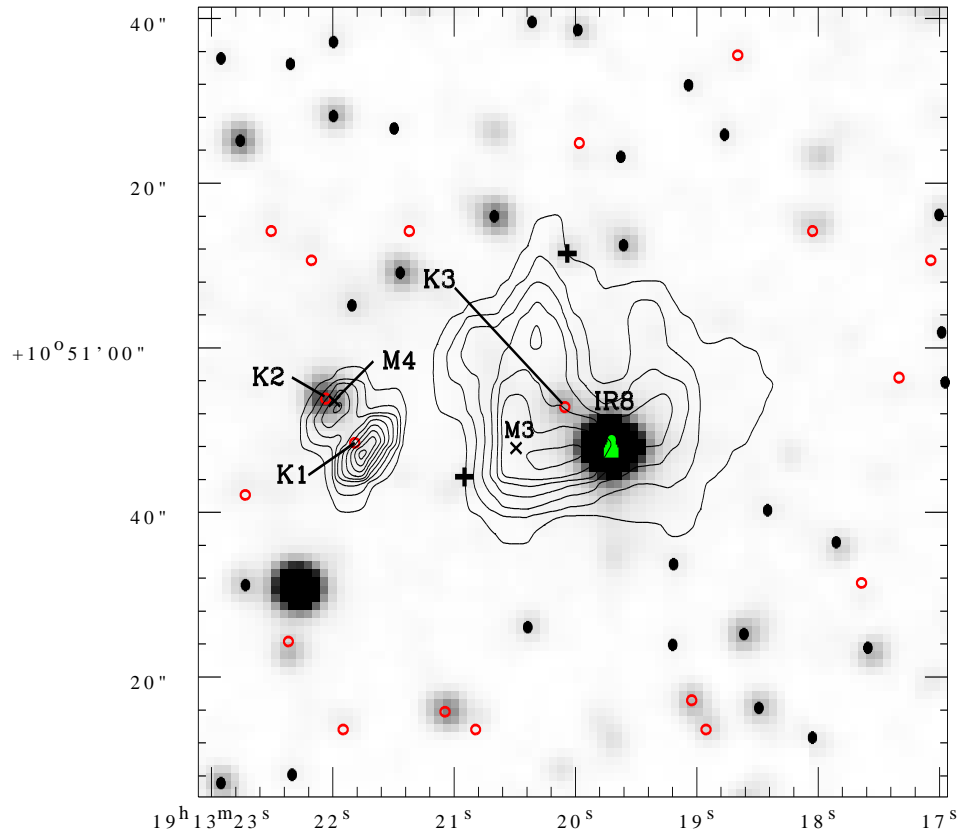


Fig. 15.— Same as in Fig 14 but for the region around IRAS 19110+1045. The open circles indicate the sources detected only in H and  $K_s$  bands or only in  $K_s$ -band.